Dynamic compartmentalization of the pro-invasive transcription factor NHR-67 reveals a role for Groucho in regulating a proliferative-invasive cellular switch in *C. elegans*

Authors: Taylor N. Medwig-Kinney[1†*], Brian A. Kinney[2†], Michael A. Q. Martinez[1], Callista Yee[3], Sydney S. Sirota[1‡], Angelina A. Mullarkey[1], Neha Somineni[1§], Justin Hippler[1,4#], Wan Zhang[1], Kang Shen[3], Christopher M. Hammell[2], Ariel M. Pani[5], and David Q. Matus[1¶*]

Affiliations:

1. Department of Biochemistry and Cell Biology, Stony Brook University, Stony Brook, NY 11794, United States.
2. Cold Spring Harbor Laboratory, Cold Spring Harbor, NY 11724, United States.
3. Howard Hughes Medical Institute, Department of Biology, Stanford University, Stanford, CA 94305, United States.
4. Science and Technology Research Program, Smithtown High School East, St. James, NY 11780, United States.
5. Departments of Biology and Cell Biology, University of Virginia, Charlottesville, VA 22904, United States.

***For correspondence:** tmkinney@unc.edu; david.matus@stonybrook.edu

Present address: [†]Department of Biology, University of North Carolina at Chapel Hill, Chapel Hill, NC 27599, United States; [‡]Touro College of Osteopathic Medicine, Middletown, NY 10940, United States; [§]Integra LifeSciences, Princeton, NJ 08540, United States; [#]Northeastern University, Boston, MA 02115, United States; [¶]Arcadia Science, Berkeley, CA 94704, United States.

Competing interest: David Q. Matus and Neha Somineni are paid employees of Arcadia Science and Integra LifeSciences, respectively.

Abstract

A growing body of evidence suggests that cell division and basement membrane invasion are mutually exclusive cellular behaviors. How cells switch between proliferative and invasive states is not well understood. Here, we investigated this dichotomy *in vivo* by examining two cell types in the developing *Caenorhabditis elegans* somatic gonad that derive from equipotent progenitors, but exhibit distinct cell behaviors: the post-mitotic, invasive anchor cell and the neighboring proliferative, non-invasive ventral uterine (VU) cells. We show that the fates of these cells post-specification are more plastic than previously appreciated and that levels of NHR-67 are important for discriminating between invasive and proliferative behavior. Transcription of *nhr-67* is downregulated following post-translational degradation of its direct upstream regulator, HLH-2 (E/Daughterless) in VU cells. In the nuclei of VU cells, residual NHR-67 protein is compartmentalized into discrete punctae that are dynamic over the cell cycle and exhibit liquid-like properties. By screening for proteins that colocalize with NHR-67 punctae, we identified new regulators of uterine cell fate maintenance: homologs of the transcriptional co-repressor Groucho (UNC-37 and LSY-22), as well as the TCF/LEF homolog POP-1. We propose a model in which association of NHR-67 with the Groucho/TCF complex suppresses the default invasive state in non-invasive cells, which complements transcriptional regulation to add robustness to the proliferative-invasive cellular switch *in vivo*.

Introduction

Cellular proliferation and invasion are key aspects of development (reviewed in Medwig & Matus, 2017), and are also two of the defining hallmarks of cancer (reviewed in Hanahan and Weinberg, 2000). A growing body of evidence suggests that cell cycle progression and invasion through a basement membrane are mutually exclusive cellular behaviors in both development and disease states (reviewed in Kohrman and Matus, 2017). Switching between invasive and proliferative phenotypes has been observed in melanoma and recently in breast cancer (Hoek et al., 2008; Mondal et al., 2021), but

how these cell states are regulated in the context of development is not well understood. To investigate how this dichotomy in cellular behavior is controlled *in vivo*, we used *C. elegans*, leveraging its highly stereotypical development (Sulston and Horvitz, 1977), as well as its genetic and optical tractability. During development of the hermaphroditic reproductive system, the proximal granddaughters of the Z1 and Z4 somatic gonad progenitors, Z1.pp and Z4.aa, give rise to four cells that will adopt one of two cellular fates: a proliferative ventral uterine (VU) cell or the terminally differentiated, invasive anchor cell (AC) (Figure 1A) (Kimble and Hirsh, 1979). The distal cells of this competency group, Z1.ppa and Z4.aap, quickly lose their bipotentiality and become VU cells (Seydoux et al., 1990). In contrast, the proximal cells, Z1.ppp and Z4.aaa, undergo a stochastic Notch-mediated cell fate decision, giving rise to another VU cell and the post-mitotic AC (Figure 1A,B) (Greenwald et al., 1983; Seydoux and Greenwald, 1989). Following fate specification, the AC undergoes invasive differentiation and breaches the underlying basement membrane, connecting the uterus to the vulval epithelium to facilitate egg-laying (Figure 1B) (Sherwood and Sternberg, 2003). The AC is the default cell fate of the somatic gonad, as disruption of Notch or Wnt signaling results in ectopic AC specification (Phillips et al., 2007; Seydoux and Greenwald, 1989). Therefore, AC fate must be actively repressed.

Our previous work has shown that AC invasion is dependent on G_0 cell cycle arrest, which is coordinated by the pro-invasive transcription factor NHR-67 (NR2E1/TLX) (Figure 1–figure supplement 1A) (Matus et al., 2015). NHR-67 functions within a gene regulatory network comprised of four conserved transcription factors whose homologs have been implicated in several types of metastatic cancer (Liang and Wang, 2020; Milde-Langosch, 2005; Nelson et al., 2021; Wang and Baker, 2015). We previously reported that NHR-67 is regulated by a feed-forward loop formed by EGL-43 (Evi1) and HLH-2 (E/Daughterless), which functions largely in parallel to a cell cycle-independent subcircuit controlled by FOS-1 (Fos) (Figure 1–figure supplement 1A) (Medwig-Kinney et al., 2020). EGL-43, HLH-2, and NHR-67 are reiteratively used within the Z lineage of the somatic gonad, in that they also function to independently regulate LIN-12 (Notch) signaling during the initial AC/VU cell fate decision (Medwig-Kinney et al., 2020). Despite its role in lateral inhibition between Z1.ppp and Z4.aaa, expression of

93 LIN-12 is not absolutely required for VU cell fate (Sallee et al., 2015). Cell cycle state
94 also cannot explain the difference between AC and VU cell fates, as arresting VU cells
95 in G_0 through ectopic expression of CKI-1 (p21/p27) does not make them invasive
96 (Smith et al., 2022). Thus, the mechanisms responsible for maintaining AC and VU
97 cellular identities following initial cell fate specification remain unclear.
98 Maintenance of differentiated cell identity is essential for ensuring tissue integrity
99 during development and homeostasis, and the inability to restrict phenotypic plasticity is
100 now being recognized as an integral part of cancer pathogenesis (Hanahan, 2022). *In*
101 *vitro* studies have identified several factors that safeguard differentiated cell identity
102 (reviewed in Brumbaugh et al., 2019). Despite its largely autonomous modality of
103 development, *C. elegans* has emerged as an ideal model system to study cell fate
104 maintenance *in vivo*. There have been several reports of cell fate transformations that
105 occur naturally, including two epithelial-to-neural transdifferentiation events (Jarriault et
106 al., 2008; Riva et al., 2022), or following fate challenges (reviewed in Rothman and
107 Jarriault, 2019). In such contexts, several epigenetic factors, including chromatin
108 remodelers and histone chaperones, have been identified for their roles in restricting
109 cell fate reprogramming (Hajduskova et al., 2019; Kagias et al., 2012; Kolundzic et al.,
110 2018; Patel et al., 2012; Rahe and Hobert, 2019; Zuryn et al., 2014). However, in some
111 cases, ectopic expression of a specific transcription factor is sufficient to overcome
112 these barriers, as was first shown through pioneering work in mouse embryonic
113 fibroblasts (Davis et al., 1987). Indeed, there are several examples in *C. elegans* where
114 ectopic expression of single lineage-specific transcription factors induces cell fate
115 transformations (Fukushige and Krause, 2005; Gilleard and McGhee, 2001; Horner et
116 al., 1998; Jin et al., 1994; Kiefer et al., 2007; Quintin et al., 2001; Richard et al., 2011;
117 Riddle et al., 2013; Tursun et al., 2011; Zhu et al., 1998). Moreover, *C. elegans* uterine
118 tissue may be particularly amenable to fate transformations, as ectopic expression of a
119 single GATA transcription factor, ELT-7, is sufficient to induce transorganogenesis of
120 the somatic gonad into gut by reprogramming the mesodermally-derived tissue into
121 endoderm (Riddle et al., 2016). Valuable insights have been made into how the function
122 of fate-specifying transcription factors can be tuned through means such as
123 autoregulation and dynamic heterodimerization (Leyva-Díaz and Hobert, 2019; Sallee et

124 al., 2017). We are just beginning to understand how an additional layer of control over
125 transcriptional regulators can be achieved through compartmentalization (Boija et al.,
126 2018; Lim and Levine, 2021).
127 Here, in our endeavor to understand how AC and VU cellular fates are
128 maintained, we identified two mechanisms that together modulate the invasive-
129 proliferative switch in *C. elegans*. We found that high levels of NHR-67 expression are
130 sufficient to drive invasive differentiation, and that *nhr-67* is transcriptionally
131 downregulated in the non-invasive VU cells following the post-translational degradation
132 of its direct upstream regulator, HLH-2. Additionally, we observed that remaining NHR-
133 67 protein in the VU cells compartmentalizes into punctae that exhibit liquid-like
134 properties including dynamic assembly, fusion, and dissolution over cell cycle as well as
135 rapid recovery kinetics after photobleaching. These NHR-67 punctae colocalize *in vivo*
136 with UNC-37 and LSY-22, homologs of the transcriptional co-repressor Groucho, as
137 well as with POP-1 (TCF/LEF), which is likely mediated through a direct interaction
138 between UNC-37 and the intrinsically disordered C-terminal region of NHR-67. Through
139 functional perturbations, we demonstrate that UNC-37, LSY-22, and POP-1 contribute
140 to repression of the default invasive state in VU cells. We propose a model in which
141 NHR-67 compartmentalizes through its interaction with Groucho, which, combined with
142 transcriptional downregulation of *nhr-67*, may suppress invasive differentiation.
143
144 **Results**
145
146 **NHR-67 expression levels are important for distinguishing AC and VU cell identity**
147 Despite arising from initially equipotent cells, the differentiated AC and VU cells
148 exhibit very distinct cellular behaviors. The AC terminally differentiates to invade the
149 underlying basement membrane while the VU cells remain proliferative, undergoing
150 several rounds of division before terminally differentiating. One potential explanation for
151 this difference in cell behavior is asymmetric expression of pro-invasive transcription
152 factors. To investigate this possibility, we examined endogenous expression levels of
153 four transcription factors that function in the gene regulatory network coordinating AC
154 invasion (EGL-43, FOS-1, HLH-2, and NHR-67) using GFP-tagged alleles (Medwig-

155 Kinney et al., 2020). While FOS-1 levels are enriched in the AC compared to the VU
156 cells (Figure 1–figure supplement 1B,C), FOS-1 has no known role in cell cycle
157 regulation, so we did not pursue this protein further (Medwig-Kinney et al., 2021). EGL-
158 43 was also not a promising candidate, as it is expressed in both cell types at
159 comparable levels, with VU cells exhibiting approximately 89% of AC expression (Figure
160 1–figure supplement 1B,C). In contrast, HLH-2 exhibits significant asymmetry in
161 expression, as VU cells express merely 17% of HLH-2 levels observed in the AC
162 (Figure 1C,D). Previous studies have shown that dimerization-driven degradation of
163 HLH-2 is responsible for its downregulation in the VU cells (Benavidez et al., 2022; Karp
164 and Greenwald, 2003; Sallee and Greenwald, 2015). NHR-67 exhibits a similar pattern
165 of expression with over three-fold enrichment in the AC, consistent with prior
166 observations of transgenic reporters (Figure 1C,D) (Verghese et al., 2011). Given the
167 known role of NHR-67 in regulating cell cycle and invasion, we hypothesized that its
168 differential expression between the AC and VU cells could contribute to their distinct
169 cellular behaviors.
170 To assess the potential role of NHR-67 in regulating uterine cell identities, we
171 manipulated its expression levels. We found that strong depletion of NHR-67 through
172 RNA interference (RNAi) treatment results in ACs adopting VU-like characteristics.
173 During AC/VU cell fate specification, LIN-12 (Notch) normally becomes restricted to the
174 VU cells while the Delta-like ligand LAG-2 (visualized by LAG-
175 2::P2A::H2B::mTurquoise2 (Medwig-Kinney et al., 2022)) accumulates in the AC
176 (Wilkinson et al., 1994). Here, we observe that NHR-67 deficient ACs not only
177 proliferated and failed to invade, as reported previously (Matus et al., 2015), but also
178 ectopically expressed membrane-localized Notch (visualized by LIN-12::mNeonGreen
179 (Pani et al., 2022)) (Figure 1E; Figure 1–figure supplement 2A,B). Notably, NHR-67-
180 deficient ACs expressed both LIN-12 and LAG-2, potentially indicating an intermediate
181 state between AC and VU cell fate (Figure 1E; Figure 1–figure supplement 2A,B). Next,
182 we ectopically expressed NHR-67 ubiquitously following AC/VU specification using a
183 heat shock inducible transgene (*hsp*::NHR-67::2x-BFP) (Medwig-Kinney et al., 2020)
184 and observed the presence of multiple invasive ACs at a low penetrance (approximately
185 5%, n > 50), denoted by ectopic expression of an AC marker (*cdh*-

186 *3p*::mCherry::moeABD) and expansion of the basement membrane gap (Figure 1F). As
187 previous work has demonstrated that proliferative ACs cannot invade (Matus et al.,
188 2015), we concluded that these invasive ectopic ACs most likely arose from fate
189 conversion of neighboring VU cells. Taken together, these pieces of evidence suggest
190 that high and low levels of NHR-67 correlate to properties of AC and VU cell identities,
191 respectively (Figure 1G).
192
193 **NHR-67 is enriched in the AC through transcriptional regulation by HLH-2**
194 Next, we investigated how NHR-67 expression levels become asymmetric
195 between the AC and VU cells. We and others have previously shown that HLH-2
196 positively regulates NHR-67 expression in the context of the AC (Figure 1–figure
197 supplement 1A) (Bodofsky et al., 2018; Medwig-Kinney et al., 2020). If this regulatory
198 interaction also exists in the context of the VU cells, it could explain why the relative
199 expression pattern of NHR-67 in the AC and VU cells mirrors that of HLH-2. In support
200 of this hypothesis, we found that initial onset of HLH-2, which has shown to be
201 asymmetric in Z1.pp and Z4.aa (Attner et al., 2019), correlates to that of NHR-67 onset
202 (Figure 2–figure supplement 1A). To test whether HLH-2 degradation is responsible for
203 NHR-67 downregulation in the VU, we drove ectopic expression of HLH-2 using a
204 transgene under the control of a heat shock inducible promoter (*hsp*::HLH-2::2x-BFP)
205 (Medwig-Kinney et al., 2020) and observed elevated NHR-67 expression in VU cells
206 (43% increase; n > 30) (Figure 2A,B). To control against potential dimerization-driven
207 degradation of HLH-2 in the VU cells, which the heat shock inducible transgene would
208 still be susceptible to, we disrupted UBA-1, an E1 ubiquitin-activating enzyme that has
209 recently been shown to be necessary for HLH-2 degradation in VU cells (Benavidez et
210 al., 2022). Following perturbation of UBA-1 through RNAi treatment, HLH-2 expression
211 in the VU cells increased more than four-fold and NHR-67 expression increased by
212 nearly 60% compared to the empty vector control (Figure 2–figure supplement 1B-D).
213 Both experiments suggest that *nhr-67* expression in the VU cells is at least partially
214 regulated by levels of HLH-2.
215 It has previously been proposed that the interaction between HLH-2 and *nhr*-67
216 is direct. This is based on the identification of E binding motifs within a 276 bp region of

217 the *nhr-67* promoter that is required for NHR-67 expression in the uterine tissue and
218 encompasses the location of several hypomorphic mutations (*pf2*, *pf88*, *pf159*) (Figure
219 2C) (Bodofsky et al., 2018; Verghese et al., 2011). We performed a yeast one-hybrid
220 assay by generating a bait strain containing this *nhr-67* promoter region and pairing it
221 with an HLH-2 Gal4-AD prey plasmid from an existing yeast one-hybrid library (Reece-
222 Hoyes et al., 2005). Yeast growth on the selective SC-HIS-TRP plates containing the
223 competitive inhibitor 3-aminotriazole (3-AT) suggests that HLH-2 is capable of binding
224 directly to this 276 bp region of the *nhr-67* promoter (Figure 2D). Together, these results
225 support that direct transcriptional regulation of *nhr-67* by HLH-2 contributes to the
226 asymmetry in NHR-67 expression between the AC and VU cells.
227
228 **NHR-67 dynamically compartmentalizes in VU cell nuclei**
229 Upon closer examination of GFP-tagged NHR-67, it became evident that the AC
230 and VU cells not only exhibit differences in overall NHR-67 levels, but also in
231 localization of the protein. While NHR-67 localization is fairly uniform throughout the AC
232 nucleus (excluding the nucleolus), we often observed discrete punctae throughout the
233 nuclei of VU cells (Figure 3A,B). These punctae were observed with NHR-67
234 endogenously tagged with several different fluorescent proteins, including GFP,
235 mNeonGreen, mScarlet-I, and TagRFP-T (Figure 3–figure supplement 1A,B) and in the
236 absence of tissue fixation methods that can cause artificial puncta (Irgen-Gioro et al.,
237 2022), suggesting that they are not an artifact of the fluorophore or sample preparation.
238 To characterize dynamics of these punctae during interphase states of the cell
239 cycle, we paired GFP-tagged NHR-67 with a CDK activity sensor. The CDK activity
240 sensor is comprised of a fragment of DNA Helicase B (DHB) fused to a fluorophore (2x-
241 mKate2), expressed under a ubiquitous promoter (Figure 3C) (Adikes et al., 2020). DHB
242 contains a strong nuclear localization signal (NLS), flanked by four serine sites, as well
243 as a weaker nuclear export signal (NES). As CDK activity increases over the cell cycle,
244 the CDK sensor is translocated from the nucleus to the cytoplasm, allowing for
245 correlation of its relative subcellular localization to cell cycle state (Figure 3C) (Adikes et
246 al., 2020; Spencer et al., 2013). Time-lapse microscopy revealed that the number of
247 NHR-67 punctae was dynamic over the course of the cell cycle, with punctae first

248 appearing shortly after mitotic exit in the G1 phase, and then reducing in number to two
249 large punctae prior to nuclear envelope breakdown before disappearing (Figure 3D,E).
250 We collected additional recordings with finer time resolution and captured fusion, or
251 condensation, of punctae prior to their dissolution (representative of 6 biological
252 replicates) (Figure 3F). These punctae also exhibit relatively rapid diffusion kinetics, as
253 observed by fluorescence recovery following photobleaching ($t_{1/2}$ = 46 seconds; n = 8)
254 at a rate within the same order of magnitude as P granule proteins PGL-1 and PGL-3
255 (Figure 3G,H) (Putnam et al., 2019).
256
257 **Groucho homologs UNC-37 and LSY-22 associate with NHR-67 punctae and**
258 **contribute to VU cell fate**
259 Next, we tested the extent to which NHR-67 punctae colocalize with homologs of
260 other proteins known to compartmentalize in nuclei by pairing GFP- and mScarlet-I-
261 tagged NHR-67 with other endogenously tagged alleles. As NHR-67 is a transcription
262 factor, we speculated that its punctae may represent clustering around sites of active
263 transcription, which would be consistent with data showing RNA Polymerase II and the
264 Mediator complex can compartmentalize with transcription factors (Cho et al., 2018). To
265 test this hypothesis, we co-visualized NHR-67 with a GFP-tagged allele of *ama-1*, the
266 amanitin-binding subunit of RNA polymerase II (Hills-Muckey et al., 2021) and failed to
267 observe significant colocalization between NHR-67 and AMA-1 punctae (Manders'
268 overlap coefficient, M = 0.066) compared to negative controls where a single channel
269 was compared to its 90-degree rotation (M = 0.108) (Figure 4A,B). Another possibility
270 considered is that NHR-67 punctae could correlate to chromatin organization, as
271 heterochromatin has been shown to be compartmentalized in the nucleus (Larson et al.,
272 2017; Strom et al., 2017). However, we did not observe significant colocalization of
273 NHR-67 with the endogenously tagged HP1 heterochromatin proteins (Patel and
274 Hobert, 2017) HPL-1 (M = 0.076) or HPL-2 (M = 0.083) (Figure 4A,B). We next tested if
275 NHR-67 colocalizes with the transcriptional co-repressor Groucho, as Groucho had
276 recently been shown to compartmentalize in the nuclei of cells in *Ciona* (Treen et al.,
277 2021). The *C. elegans* genome encodes one Groucho homolog, UNC-37, which we
278 acquired an mNeonGreen-tagged allele of (Ma et al., 2021), and a Groucho-like protein,

279 LSY-22, which we tagged with TagRFP-T (Figure 4–figure supplement 1). We observed
280 significant colocalization of NHR-67 punctae with both LSY-22 (M = 0.686) and UNC-37
281 (M = 0.741), comparable to colocalization measures in heterozygous NHR-
282 67::mScarlet-I/NHR-67::GFP animals (M = 0.651), which were used as positive controls
283 (Figure 4A,B). This evidence suggests that NHR-67 punctae do not localize to sites of
284 active transcription or chromatin compaction, but instead associate with transcriptional
285 co-repressors.
286 Since the AC is the default state of the AC/VU cell fate decision (Seydoux and
287 Greenwald, 1989), we hypothesized that the punctae including NHR-67, UNC-37, and
288 LSY-22 may function in repressing invasive differentiation. To test this hypothesis, we
289 depleted UNC-37 and LSY-22 utilizing the auxin inducible degron (AID) protein
290 degradation system, in which a protein of interest is tagged with an AID that is
291 recognized by TIR1 in the presence of auxin and ubiquitinated by the SCF E3 ubiquitin
292 ligase complex (Figure 4C) (Martinez et al., 2020; Zhang et al., 2015). We re-tagged
293 LSY-22 with mNeonGreen::AID (Figure 4–figure supplement 1) and acquired a
294 BFP::AID-tagged allele of *unc-37* (Kurashina et al., 2021). Each AID-tagged allele was
295 paired with a transgene encoding *Arabidopsis thaliana* TIR1 ($_{At}$TIR1) that was co-
296 expressed with a nuclear-localized mCherry::HIS-11. Following auxin treatment, we
297 observed ectopic expression of an AC marker (*cdh-3p*::mCherry::moeABD) in 28% of
298 LSY-22::AID animals and 59% of UNC-37::AID animals (n = 64 for both) (Figure 4D,E).
299 These results are consistent with phenotypes we observed in genetic backgrounds with
300 *unc-37* hypomorphic (*unc-37(e262wd26)*) and null (*unc-37(wd17wd22)*) mutant alleles
301 (Figure 4–figure supplement 2). It is likely that dual depletion of UNC-37 and LSY-22
302 would result in a higher penetrance of ectopic ACs given their partial redundancy in
303 function (Flowers et al., 2010), but animals possessing both AID-tagged alleles were not
304 viable when paired with the $_{At}$TIR1 transgene.
305
306 **TCF/LEF homolog POP-1 associates with NHR-67 punctae and contributes to VU**
307 **cell fate post-specification**
308 While UNC-37 and LSY-22 appear to be important for maintenance of normal
309 uterine cell fates, both genes are broadly expressed and exhibit comparable levels

310 (<10% difference) between the AC and VU cells (Figure 5A,C; Figure 5–figure
311 supplement 1A,B); therefore, we hypothesized that another factor must be involved. It
312 had previously been reported that the sole TCF/LEF homolog in *C. elegans*, POP-1,
313 forms a repressive complex with UNC-37 in the early embryo to restrict expression of
314 the endoderm-determining gene, END-1 (Calvo et al., 2001). Additionally, POP-1 has a
315 known role in development of the somatic gonad, as perturbing its function results in
316 ectopic ACs (Siegfried and Kimble, 2002). Examination of an eGFP-tagged *pop-1* allele
317 (van der Horst et al., 2019), showed significant enrichment in the VU cells (>20%)
318 compared to the AC (Figure 5B,C; Figure 5–figure supplement 1A,B). We also observed
319 that endogenous POP-1 forms punctae in the nuclei of VU cells, which had previously
320 been observed during interphase in non-Wnt signaled embryonic cells (Maduro et al.,
321 2002). These POP-1 punctae colocalize with NHR-67 (M = 0.547), although to a lesser
322 degree than UNC-37 and LSY-22, likely because the strong POP-1 fluorescence
323 outside of punctae made them more difficult to segment (Figure 5D,E). Additionally, *nhr-*
324 *67(RNAi)* treatment resulted in a significant increase in AC expression of eGFP::POP-1
325 compared to empty vector controls (225%, n > 30), a pattern we observed following
326 depletion of other transcription factors (Medwig-Kinney et al., 2020) and chromatin
327 modifiers (Smith et al., 2022) required for AC arrest and invasion (Figure 5F,G; Figure
328 5–figure supplement 2A,B). This negative regulation of POP-1 by NHR-67 may explain
329 why the proteins have opposite patterns of enrichment.
330 It has previously been suggested that POP-1 may be functioning as an activator
331 in the VU precursors Z1.ppa and Z4.aap based on the relative expression of a POP-1
332 transgene (Sallee et al., 2015). This view is largely dependent on the notion that high
333 levels of POP-1 correlate to repressive function and low levels are conducive for
334 activator roles (Shetty et al., 2005). In contrast, we did not find evidence of
335 transcriptional activation by POP-1 in the AC/VU precursors nor their differentiated
336 descendants using an established POPTOP (POP-1 and TCF optimal promoter)
337 reporter, which contains seven copies of POP-1/TCF binding sites and the *pes-10*
338 minimal promoter (Figure 5H; Figure 5–figure supplement 3A,B) (Green et al., 2008).
339 The growing consensus regarding the Wnt/β-catenin asymmetry pathway is that relative
340 levels of POP-1 and β-catenin are more important than absolute protein levels of POP-1

341 (Phillips and Kimble, 2009). Our proposed model of POP-1 acting as a repressor in the
342 proximal gonad is consistent with the finding that SYS-1 (β-catenin) expression is
343 restricted to the distal gonad early in somatic gonad development and is not detectable
344 in the AC or VU cells (Figure 5–figure supplement 3C) (Phillips et al., 2007; Sallee et al.,
345 2015). It is also supported by recent evidence suggesting that UNC-37/LSY-22 mutant
346 alleles phenocopy *pop-1* knockdown, which produces ectopic distal tip cells (Bekas and
347 Phillips, 2022).

348 One aspect that makes studying the repressive role of POP-1 in cell fate
349 maintenance challenging is that its activator function is required for distal cell fate
350 specification in the somatic gonad earlier in development. Loss of either POP-1 and
351 SYS-1 results in a Sys (symmetrical sister cell) phenotype, where all somatic gonad
352 cells adopt the default proximal fate and thereby give rise to ectopic ACs (Siegfried and
353 Kimble, 2002; Siegfried et al., 2004). This likely occluded previous identification of the
354 potential repressive role of POP-1 in maintaining VU cell fates. To achieve temporal
355 control over POP-1 expression to tease apart its roles, we sought to use the AID
356 system, but insertion of the degron into the *pop-1* locus disrupted the protein's function.
357 Instead, we paired eGFP-tagged POP-1 with a uterine-specific anti-GFP nanobody
358 (Smith et al., 2022; Wang et al., 2017). The anti-GFP nanobody is fused to ZIF-1 and
359 serves as an adapter, recognizing GFP-tagged proteins and promoting their
360 ubiquitination by the Cullin2-based E3 ubiquitin ligase, which ultimately targets them for
361 degradation via the proteasome (Figure 6–figure supplement 1A) (Wang et al., 2017).
362 This anti-GFP nanobody, visualized by nuclear expression of mCherry, was not
363 detectable prior to or even shortly after the AC/VU cell fate decision, which allowed us
364 to bypass disruption of initial cell specification (Figure 6–figure supplement 1B). While
365 this method only produced a mild knockdown of POP-1 in the VU cells, we still observed
366 the ectopic AC phenotype at low penetrance (7%, n = 60) (Figure 6–figure supplement
367 1C). To achieve stronger depletion, we used RNAi for further POP-1 perturbations.

368 To interrogate the phenotypic consequences of POP-1 perturbation, we utilized a
369 strain expressing two markers of AC fate (*cdh-3p*::mCherry::moeABD and LAG-
370 2::P2A::H2B::mTurquoise2). Following treatment with *pop-1(RNAi)*, we observed
371 several animals with two or more bright *cdh-3/lag*-2+ ACs, consistent with known

372 phenotypes caused by cell fate misspecification in the somatic gonad (17%, n = 30)
373 (Figure 6A). We also observed animals with invasive cells that express AC markers at
374 different levels (53%, n = 30), suggesting that the cells did not adopt AC fate at the
375 same time (Figure 6A). To test whether the subset of dim *cdh-3/lag-2*+ ACs are the
376 result of VU-to-AC cell fate conversion, we visualized AC and VU fates simultaneously
377 using the AC markers previously described along with an mNeonGreen-tagged allele of
378 *lag-1* (CSL), a protein downstream of Notch signaling whose expression becomes
379 restricted to the VU cells following AC/VU cell fate specification. Following treatment
380 with *pop-1(RNAi)*, we found that a subset of ectopic ACs co-express AC markers and
381 LAG-1, likely indicating an intermediate state between the two cell types (Figure 6–
382 figure supplement 2). To visualize this process live, we used time-lapse microscopy and
383 were able to capture ectopic ACs gradually upregulating LAG-2 (+51%, n = 3) and
384 downregulating LAG-1 (-16%, n = 3) over time (Figure 6B,C), consistent with VU-to-AC
385 cell fate conversion.
386
387 **IDR of NHR-67 facilitates protein-protein interaction with UNC-37**
388 Given that UNC-37, LSY-22, and POP-1 phenocopy each other with respect to
389 AC/VU fates and all three colocalize with NHR-67 punctae, we next sought to further
390 characterize the interactions among these proteins. Previous work has either directly
391 identified or predicted protein-protein interactions among POP-1, UNC-37, and LSY-22
392 (Boxem et al., 2008; Calvo et al., 2001; Flowers et al., 2010; Reece-Hoyes et al., 2005;
393 Simonis et al., 2009; Zhong and Sternberg, 2006). Using a yeast two-hybrid assay with
394 UNC-37 Gal4-AD prey, we confirmed that UNC-37 directly interacts with both POP-1
395 and LSY-22 after observing yeast growth on the selective SC-HIS-TRP-LEU plates
396 containing 3-AT (Figure 7–figure supplement 1). Using the same technique, we found
397 that NHR-67 binds directly to UNC-37, as previously predicted (Li et al., 2004; Simonis
398 et al., 2009), but found no evidence of it directly interacting with LSY-22 or POP-1
399 (Figure 7–figure supplement 1).
400 To further characterize the protein-protein interaction between NHR-67 and
401 UNC-37, we assessed the protein structure of NHR-67 using AlphaFold, an artificial
402 intelligence-based protein structure prediction tool (Jumper et al., 2021; Varadi et al.,

403 2022), and PONDR, a predictor of intrinsic disorder (Peng and Zhang, 2006). Both
404 identify an intrinsically disordered region (IDR) at the C-terminus of NHR-67 (Figure
405 7A,B). IDRs are low complexity domains that lack fixed three-dimensional structure and
406 have been shown to support dynamic protein-protein interactions (Chong et al., 2018).
407 To determine if the IDR of NHR-67 is important for facilitating its interaction with UNC-
408 37, we repeated the yeast two-hybrid experiment using UNC-37 Gal4-AD prey, pairing it
409 with different fragments of the NHR-67 protein: full-length, without its IDR (ΔIDR), and
410 its IDR alone (Figure 7C,D). Yeast growth on the selective SC-HIS-TRP-LEU plates
411 containing the competitive inhibitor 3-aminotriazole (3-AT) demonstrates that the 108
412 amino acid IDR sequence of NHR-67 is necessary and sufficient to bind with UNC-37
413 (Figure 7C,D).
414 Thus, we propose the following potential model of *C. elegans* uterine cell fate
415 maintenance based on the data presented here and known roles of Groucho and TCF
416 proteins in regulating transcription . First, transcription of *nhr-67* is directly regulated by
417 HLH-2, resulting in its enrichment in the AC compared to the VU cells. In the AC, where
418 NHR-67 levels are high and POP-1 is repressed, NHR-67 is free to activate genes
419 promoting invasive differentiation. In the VU cells, where NHR-67 levels are low and
420 POP-1 levels are high, POP-1 assembles with LSY-22, UNC-37, and NHR-67, either
421 directly repressing NHR-67 targets or sequestering NHR-67 away from its targets
422 (Figure 7E). It is possible that POP-1 negatively regulates NHR-67 at the transcriptional
423 level as well, as the *nhr-67* promoter contains 7 putative TCF binding sites (Zacharias et
424 al., 2015).
425
426 **Discussion**
427
428 In summary, here we provide evidence that activity of the pro-invasive
429 transcription factor, NHR-67, is simultaneously regulated by two distinct processes,
430 which together modulate the proliferative-invasive switch in *C. elegans*. We show that
431 NHR-67 is a potent fate-specifying transcription factor, in that its expression is sufficient
432 for invasive differentiation of ACs in the somatic gonad. The compartmentalization of
433 NHR-67 in the VU cells could serve as a potential mechanism to suppress its function in

434 activating the pro-invasive program. We also discovered that NHR-67 forms nuclear foci
435 in non-invasive cells, which exhibit liquid-like properties, indicated by observations of
436 their condensation, dissolution, and relatively rapid recovery from photobleaching,
437 similar to what has been described with P granules (Brangwynne et al., 2009). These
438 NHR-67 punctae associate with Groucho homologs, UNC-37 and LSY-22, likely through
439 a direct protein-protein interaction with UNC-37 mediated by the C-terminal IDR of
440 NHR-67. We postulate that this association leads to protein condensation, as has
441 recently been described in *Ciona* embryos (Treen et al., 2021). Furthermore, repression
442 of the default invasive state appears to be dependent on expression of the TCF/LEF
443 homolog POP-1, which clarifies our understanding of the dual roles this protein plays
444 during development of the somatic gonad. It is also interesting to note that the dynamic
445 punctae formed by POP-1 in non-Wnt signaled cells was first described 20 years ago
446 (Maduro et al., 2002), but their function are only now being appreciated in light of recent
447 advances in our understanding of the formation of higher order associations in the
448 nucleus.
449 With regard to protein compartmentalization in the nucleus, most research has
450 been through the lens of transcriptional activation through RNA Polymerase II and the
451 mediator complex (Boija et al., 2018; Cho et al., 2018; Sabari et al., 2018) or repression
452 through HP1 heterochromatin proteins (Larson et al., 2017; Strom et al., 2017). Here we
453 report the second observed case of compartmentalization of Groucho proteins (Treen et
454 al., 2021), which may suggest that Groucho proteins have evolutionarily conserved
455 roles that require this type of subnuclear organization.
456 Still, as this is one of the first studies into compartmentalization of transcriptional
457 repressors *in vivo*, there is much left to learn. For example, it is unknown whether DNA
458 binding is necessary for nuclear puncta formation. The interaction between UNC-37 and
459 NHR-67 does not appear to depend on DNA binding, as the C-terminal IDR region of
460 NHR-67 (excluding its zinc finger domains) was sufficient for binding with UNC-37 *in*
461 *vitro*, but it is possible that DNA binding is needed for oligomerization *in vivo*.
462 Furthermore, it remains unclear if suppression of invasive differentiation is achieved by
463 simply sequestering the pro-invasive transcription factor NHR-67 away from its
464 transcriptional targets or through direct repression of transcription. If the latter, another

465 question that arises is how the repressive complex gets recruited to specific genomic
466 sites, since POP-1 and NHR-67 are both capable of binding to DNA, and whether
467 repression is achieved through competition with transcriptional activators or recruitment
468 of histone deacetylases. Direct targets of NHR-67 have not yet been discovered, which
469 makes it difficult to investigate this specific aspect of the repressive mechanism at
470 present. We see this as a promising avenue of future study as technologies advance,
471 allowing for transcriptional profiling and target identification in specific tissues or cells
472 (Gómez-Saldivar et al., 2020; Katsanos and Barkoulas, 2022).
473 In this work, we have also identified several perturbations (i.e., increasing levels
474 of NHR-67, decreasing levels of UNC-37/LSY-22) that result in incompletely penetrant
475 transdifferentiation phenotypes and/or intermediate cell fates. We foresee these being
476 ideal cell fate challenge backgrounds in which to perform screens to identify regulators
477 of cellular plasticity, as has been done in other contexts (Rahe and Hobert, 2019).
478 Additionally, these induced fate transformations can be paired with tools to visualize and
479 manipulate cell cycle (Adikes et al., 2020) to determine if any cell cycle state is
480 particularly permissive for cell fate plasticity. While G1 arrest has been shown to
481 enhance conversion of human fibroblasts to dopaminergic neurons (Jiang et al., 2015),
482 mitosis is required for the natural K-to-DVB transdifferentiation event in *C. elegans* (Riva
483 et al., 2022). As control of proliferation and invasion, as well as maintenance of
484 differentiated cellular identities, are important for both homeostatic and disease states, it
485 is our hope that this work will shed light on how cells switch between these states in the
486 context of cancer growth and metastasis.
487
488 **Materials and methods**
489
490 ***C. elegans* strains, culture, and nomenclature**
491 Methods for *C. elegans* culture and genetics were followed as previously
492 described (Brenner, 1974). Developmental synchronization for experiments was
493 achieved through alkaline hypochlorite treatment of gravid adults to isolate eggs (Porta-
494 de-la-Riva et al., 2012). L1 stage animals were plated on nematode growth media
495 plates and subsequently cultured at 20°C or 25°C. Heat shock-inducible transgenes

496 were activated by incubating animals on plates sealed with Parafilm in a 33°C water
497 bath for 2-3 hours. In the text and in figures, promoter sequences are designated with a
498 "*p*" following the gene name and gene fusions are represented by a double-colon (::)
499 symbol.
500
501 **CRISPR/Cas9 injections**
502 New alleles and single-copy transgenes were generated by homology directed
503 repair using CRISPR-based genome engineering. mScarlet::AID and mNeonGreen::AID
504 were inserted into the C-terminus of the *nhr-67* locus by injecting adult germlines with
505 Cas9 guide-RNA ribonucleoprotein complexes and short single-stranded
506 oligodeoxynucleotide donors, as previously described (Ghanta and Mello, 2020).
507 Successful integration was identified through screening for fluorescence and by PCR.
508 The *lsy-22* locus was edited by injecting a Cas9 guide RNA plasmid and repair template
509 plasmid containing a self-excising cassette with selectable markers to facilitate
510 screening (Dickinson et al., 2015; Dickinson and Goldstein, 2016; Huang et al., 2021).
511 Repair templates used to tag *lsy-22* with TagRFP-T::AID and mNeonGreen::AID were
512 generated by cloning ~750-850 bp homology arms into pTNM063 and pDD312,
513 respectively (Ashley et al., 2021; Dickinson et al., 2015). All guide and repair sequences
514 used can be found in Supplementary File 1.
515
516 **Existing alleles**
517 The GFP-tagged alleles of the pro-invasive transcription factors *(egl-43, fos-1,*
518 *hlh-2,* and *nhr-67)* and the TagRFP-T::AID-tagged *nhr-67* allele were generated in
519 preceding work (Medwig-Kinney et al., 2021, 2020). Recent micropublications describe
520 the P2A::H2B::mTurquoise2-tagged *lag-2* and mNeonGreen-tagged *lin-12* alleles used
521 in this study (Medwig-Kinney et al., 2022; Pani et al., 2022). The eGFP-tagged *pop-1*
522 allele and POPTOP reporter were previously published (Green et al., 2008; van der
523 Horst et al., 2019), as were the AID::BFP and mNeonGreen tagged alleles of *unc-37*
524 (Kurashina et al., 2021; Ma et al., 2021). GFP-tagged *ama-1* (Hills-Muckey et al., 2021)
525 as well as mKate2-tagged *hpl-1* and *hpl-2* (Patel and Hobert, 2017) were also
526 disseminated in prior publications. The single-copy transgenes expressing the CDK

527 sensor and TIR1 variants under ubiquitously expressed ribosomal promoters (*rps-27*
528 and *rpl-28*, respectively) as well as the tissue-specific GFP-targeting nanobody are
529 described in previous work (Adikes et al., 2020; Hills-Muckey et al., 2021; Smith et al.,
530 2022; Wang et al., 2017) and are located at neutral genomic sites, ttTi4348 or ttTi5605
531 (Frøkjær-Jensen et al., 2013). The same is true for the heat shock inducible constructs
532 for HLH-2 and NHR-67 (Medwig-Kinney et al., 2020). The cadherin *(cdh-3)* anchor cell
533 reporter and basement membrane (laminin) markers have already been characterized
534 (Keeley et al., 2020; Matus et al., 2010). The following mutant alleles were obtained
535 from the *Caenorhabditis* Genetics Center: *unc-37(e262wd26)* and *unc-37(wd17wd22)*
536 (Pflugrad et al., 1997), the latter of which was maintained using the chromosome I/III
537 balancer *hT2* (McKim et al., 1993). The genotypes of all strains used in this study can
538 be found within the Key Resources Table.
539
540 **Auxin inducible protein degradation**
541 The auxin inducible degron (AID) system was used for strong depletion of
542 proteins of interest (Zhang et al., 2015). AID-tagged alleles were paired with the
543 *Arabidopsis thaliana* F-box protein, transport inhibitor response 1 ($_{At}$TIR1), and treated
544 with the water-soluble auxin 1-Naphthaleneacetic acid (K-NAA) at 1 mM concentration
545 (Martinez et al., 2020). Auxin was added to nematode growth media plates according to
546 previously published protocols (Martinez and Matus, 2020), which were then seeded
547 with OP50 *E. coli*. To achieve robust depletion, synchronized L1 stage animals were
548 directly plated on auxin plates.
549
550 **RNA interference**
551 The RNAi clones targeting *pop-1* and *uba-1* and the corresponding empty vector
552 control (L4440) were obtained from the Vidal library (Rual et al., 2004). The RNAi
553 constructs targeting the pro-invasive transcription factors (*egl-43*, *fos-1*, *hlh-2*, and *nhr-*
554 *67*) and chromatin modifiers (*pbrm-1*, *swsn-4*, and *swsn-8*) are derived from the highly
555 efficient RNAi vector T444T (Sturm et al., 2018) and were generated in preceding work
556 (Medwig-Kinney et al., 2020; Smith et al., 2022). To avoid known AC/VU cell fate

557 specification defects caused by *hlh-2* perturbations, synchronized animals were grown
558 on OP50 until the L2 stage when they were then shifted to *hlh-2* RNAi plates.
559
560 **Live-cell imaging**
561 With the exception of the FRAP experiments shown in Figure 3, all micrographs
562 were collected on a Hamamatsu Orca EM-CCD camera mounted on an upright Zeiss
563 AxioImager A2 with a Borealis-modified CSU10 Yokagawa spinning disk scan head
564 (Nobska Imaging) using 405 nm, 440 nm, 488 nm, 514 nm, and 561 nm Vortran lasers
565 in a VersaLase merge and a Plan-Apochromat 100×/1.4 (NA) Oil DIC objective.
566 MetaMorph software (Molecular Devices) was used for microscopy automation. Several
567 experiments were scored using epifluorescence visualized on a Zeiss Axiocam MRM
568 camera, also mounted on an upright Zeiss AxioImager A2 and a Plan-Apochromat
569 100×/1.4 (NA) Oil DIC objective. For static imaging, animals were mounted into a drop
570 of M9 on a 5% Noble agar pad containing approximately 10 mM sodium azide
571 anesthetic and topped with a coverslip. For long-term time-lapse imaging, animals were
572 first anesthetized in 5 mM levamisole diluted in M9 for approximately 20 minutes, then
573 transferred to a 5% Noble agar pad and topped with a coverslip sealed with VALAP
574 (Kelley et al., 2017). For short-term time-lapse imaging, the pre-anesthetization step
575 was omitted, and animals were transferred directly into a drop of 5 mM levamisole
576 solution on the slide.
577
578 **Fluorescence recovery after photobleaching**
579 FRAP experiments were performed using an Acal BFi UV Optimicroscan
580 photostimulation device mounted on a spinning disk confocal system consisting of a
581 Nikon Ti2 inverted microscope with Yokogawa CSU-W1 SoRa spinning disk. Data were
582 acquired using a Hamamatsu ORCA Fusion camera, 60x 1.27 NA water immersion
583 objection, SoRa disk, and 2.8x SoRa magnifier. Single plane images were collected
584 every 1 second.
585
586 **Yeast one-hybrid**

587 The 276 bp fragment of the *nhr-67* promoter (Bodofsky et al., 2018) was cloned
588 into the pMW2 vector, linearized by BamHI digestion. Linearized plasmid was
589 transformed into the Y1H yeast strain (as described in Reece-Hoyes and Walhout,
590 2018). Transformed yeast was plated on SC-HIS plates for three days before being
591 transformed with the HLH-2 Gal4-AD plasmid. Three colonies from each transformation
592 plate were streaked onto SC-HIS-TRP +3-aminotriazole (3-AT) plates. Protein-DNA
593 interactions were determined by visible growth on 3-AT conditions with negative growth
594 in empty vector controls after three days. Plates were imaged on a Fotodyne
595 FOTO/Analyst Investigator/FX darkroom imaging station.
596
597 **Yeast two-hybrid**
598 Plasmids containing target proteins fused to GAL-4 DNA-binding-domain + LEU
599 and GAL-4 Activation Domain + TRP were co-transformed into the pJ69-4a Y2H yeast
600 strain as previously described (Reece-Hoyes and Walhout, 2018). Transformed yeast
601 was plated on SC-TRP-LEU plates for three days. Three colonies from each
602 transformation plate were streaked onto SC-HIS-TRP-LEU 3-AT plates. Protein
603 interactions were determined by visible growth on 3-AT conditions with negative growth
604 in empty vector controls after three days. Plates were imaged as described in the
605 previous section.
606
607 **Quantification of protein expression and cell cycle state**
608 Image quantification was performed in Fiji/ImageJ (Schindelin et al., 2012).
609 Protein expression was quantified by drawing a region of interest and measuring the
610 mean gray value, then manually subtracting the mean gray value of a background
611 region of similar area to account for camera noise. For nuclear-localized proteins, the
612 region of interest was drawn around the nucleus. Membrane expression of LIN-12 was
613 measured by drawing a line (1.5 pixel thickness) along a cell's basolateral surface, to
614 distinguish between LIN-12 expression from the cell of interest and its neighbors. CDH-
615 3 expression was measured by drawing a region of interest around the cell membrane
616 excluding the nucleus (as the nuclear-localized TIR1 transgene was expressed in the
617 same channel). The CDK sensor was quantified as previously described (Adikes et al.,

618 2020). Following rolling ball subtraction (50 pixels), mean gray value is measured in a
619 region of interest drawn within the cytoplasm and one around the nucleus excluding the
620 nucleolus. The cytoplasmic-to-nuclear ratio correlates to CDK activity and is used to
621 assess cell cycle state (Adikes et al., 2020; Spencer et al., 2013). Movies were collected
622 by acquiring z-stacks at 5-minute intervals. Samples were time-aligned relative to
623 anaphase. Cells that did not undergo anaphase during the acquisition period were
624 aligned based on their DHB ratios. Animals that arrested in development (i.e., did not
625 show evidence of progressing through the cell cycle) were excluded from analysis.
626
627 **Colocalization analyses**
628 For colocalization analyses, single plane images were collected to avoid z drift
629 during acquisition and prevent photobleaching, which was often non-uniform between
630 red and green fluorophores. Micrographs were subject to background subtraction
631 (rolling ball radius = 50) followed by thresholding to segment punctae. Manders' overlap
632 coefficients (M) were calculated by measuring the extent that segmented punctae of
633 NHR-67 overlapped with that of other proteins using Just Another Colocalization Plugin
634 (JACoP) in Fiji/ImageJ (Bolte and Cordelières, 2006; Schindelin et al., 2012).
635 Heterozygous animals for *nhr-67*::mScarlet and *nhr-67*::GFP were used as positive
636 controls. These images were then re-analyzed following 90-degree rotation of one of the
637 two channels being compared, resulting in random colocalization that served as a
638 negative control.
639
640 **Data visualization and statistical analyses**
641 Representative images were processed using Fiji/ImageJ (Schindelin et al.,
642 2012). Heat maps were generated using the Fire lookup table. A power analysis was
643 performed prior to data collection to determine sample sizes (Cohen, 1992). Tests to
644 determine statistical significance of data were conducted in RStudio and plots were
645 generated using the R package ggplot2 (Wickham, 2016). Error bars represent the
646 mean ± standard deviation. Schematics of gene loci were generated using sequences
647 from WormBase (Harris et al., 2020) and the Exon-Intron Graphic Maker
648 (http://wormweb.org/exonintron). Figures were assembled in Adobe Illustrator.

Acknowledgments

We are grateful to Dr. Derek Applewhite and Aidan Teran for advice on quantification of protein colocalization. Additionally, we thank Chris Zhao for constructive comments on the manuscript. Some strains were provided by the Caenorhabditis Genetics Center, which is funded by NIH Office of Research Infrastructure Programs (P40 OD010440).

Additional information

Data and materials availability

All data generated or analyzed during this study are included in the manuscript and supporting files. New strains that have not been deposited with the *Caenorhabditis* Genetics Center will be made available upon request.

Author ORCIDs

Taylor N. Medwig-Kinney, https://orcid.org/0000-0001-7989-3291
Brian A. Kinney, https://orcid.org/0000-0001-5628-1436
Michael A. Q. Martinez, https://orcid.org/0000-0003-1178-7139
Callista Yee, https://orcid.org/0000-0002-2928-492X
Sydney S. Sirota, https://orcid.org/0000-0001-9990-3266
Angelina A. Mullarkey, https://orcid.org/0000-0002-5830-5347
Neha Somineni, https://orcid.org/0000-0001-5702-1695
Kang Shen, https://orcid.org/ 0000-0003-4059-8249
Christopher M. Hammell, https://orcid.org/0000-0002-5961-0976
Ariel M. Pani, https://orcid.org/0000-0002-9338-9750
David Q. Matus, https://orcid.org/0000-0002-1570-5025

Figure legends (supplementary figure legends are indented)

Figure 1: Invasive AC fate correlates to high levels of NHR-67. (A) Schematic of *C.*

680 *elegans* anchor cell (AC, magenta) and ventral uterine (VU, blue) cell fate specification
681 from the Z1 and Z4 somatic gonad precursor cell lineages (p, posterior daughter; a,
682 anterior daughter). (B) Micrographs depicting AC and VU cell differentiation over
683 developmental time. AC/VU precursors express LAG-2 (H2B::mTurquoise), which
684 eventually becomes restricted to the AC, whereas VU cells express LAG-1
685 (mNeonGreen) post-specification. The differentiated AC (*cdh-3p*::mCherry::moeABD)
686 then invades through the underlying basement membrane (LAM-2::mNeonGreen). (C-
687 D) Representative heat map micrographs (C) and quantification (D) of GFP-tagged
688 HLH-2 and NHR-67 expression in the AC and VU cells at the time of AC invasion. (E)
689 Expression of Notch (*lin-12*::mNeonGreen) and Delta (*lag-2*::P2A::H2B::mTurquoise2)
690 following RNAi-induced knockdown of *nhr-67* compared to empty vector control. (F)
691 Micrographs depicting the ectopic invasive ACs (*cdh-3p*::mCherry::moeABD,
692 arrowheads) and expanded basement membrane (*laminin*::GFP, arrows) gap observed
693 following heat shock induced expression of NHR-67 (*hsp*::NHR-67::2x-BFP) compared
694 to non-heat shocked controls. (G) Schematic summarizing AC and VU cell fates that
695 result from perturbations of NHR-67 levels. For all figures: asterisk (*), AC/VU
696 precursor; plus (+), VU precursor; solid arrowhead, AC; open arrowhead, VU cell;
697 arrows, basement membrane breach. Statistical significance determined by Student's t-
698 test (*$p > 0.05$, **$p > 0.01$, ***$p > 0.001$). Scale bars, 5 μm.
699
700 **Figure 1–figure supplement 1: Expression of pro-invasive transcription**
701 **factors EGL-43 and FOS-1 in the somatic gonad.** (A) Schematic of the AC
702 pro-invasive gene regulatory network comprised of four transcription factors:
703 EGL-43, FOS-1, HLH-2, and NHR-67. (B-C) Representative heat-map
704 micrographs (B) and quantification (C) of GFP-tagged EGL-43 and FOS-1
705 expression in the AC and VU cells.
706
707 **Figure 1–figure supplement 2: NHR-67-deficient ACs express both Notch**
708 **and Delta.** Quantification of Notch (LIN-12::mNeonGreen) (A) and Delta (LAG-
709 2::P2A::H2B::mTurquoise2) (B) expression in *nhr-67(RNAi)* treated ACs
710 compared to empty vector control AC and VU cells.

711

712 **Figure 2: NHR-67 expression is downregulated in VU cells through direct**
713 **transcriptional regulation by HLH-2.** (A-B) Representative heat map micrographs (A)
714 and quantification (B) of NHR-67::GFP expression in VU cells following heat shock
715 induced expression of HLH-2 (2x-BFP) compared to non-heat shocked controls. (C)
716 Schematic of a 276 bp putative regulatory element within the promoter of *nhr-67*
717 (Bodofsky et al., 2018), annotated with the location of three hypomorphic mutations
718 (*pf2*, pf88, and *pf159*). (D) Yeast one-hybrid experiment pairing HLH-2 Gal4-AD prey
719 with the 276 bp fragment of the *nhr-67* promoter as bait on SC-HIS-TRP plates with and
720 without competitive inhibitor 3-AT (175 mM).

721

722 **Figure 2–figure supplement 1: Onset of expression and regulatory**
723 **interaction between NHR-67 and HLH-2 in the somatic gonad.** (A)
724 Micrographs depicting onset of GFP-tagged HLH-2 and a wCherry-labeled NHR-
725 67 transgene (inverted to aid visualization) in Z1.pp and Z4.aa cells at early (top)
726 and late (bottom) stages. (B-D) Representative micrographs (B) and
727 quantification (C-D) of GFP-tagged HLH-2 and TagRFP-T-tagged NHR-67 in AC
728 (C) and VU cells (D) following *uba-1(RNAi)* compared to control. Insets depict
729 different z planes of the same image.

730

731 **Figure 3: NHR-67 dynamically compartmentalizes in nuclei of VU cells.** (A) Heat-
732 map maximum intensity projection of NHR-67::GFP showing protein localization in the
733 AC and VU cells. (B) Spatial color coded projection of NHR-67::GFP punctae in VU,
734 with nuclear border indicated with a dotted line. (C) Schematic of DNA Helicase B
735 (DHB) based CDK sensor and its dynamic localization over the cell cycle. (D) Graphs
736 depicting CDK activity levels and corresponding cell cycle state (top), and percentage of
737 cells exhibiting NHR-67::GFP punctae (bottom) over time, aligned to anaphase. (E)
738 Representative time-lapse of NHR-67::GFP over the course of a cell cycle, with cell
739 membranes indicated with dotted lines. (F) Time-lapse depicting NHR-67::GFP punctae
740 fusion prior to cell division. Bottom panels are pseudo-colored. (G-H) Quantification (G)
741 and representative images (H) depicting fluorescence recovery of NHR-67::GFP

742 following photobleaching of individual punctae (arrow).

743

744 **Figure 3–figure supplement 1: Knock-in alleles of *nhr-67*.** (A) Representative
745 images of VU cells exhibiting punctae formed by NHR-67 tagged with GFP,
746 mNeonGreen, mScarlet-I, and TagRFP-T. (B) Schematics of the new
747 endogenously tagged loci generated in this paper for *nhr-67*. Scale bar, 100 base
748 pairs (bp).

749

750 **Figure 4: Groucho homologs LSY-22 an UNC-37 colocalize with NHR-67 punctae**
751 **and contribute to maintenance of VU cell fate.** (A) Co-visualization of NHR-67 with
752 RNA Polymerase II (GFP::AMA-1), HP1 heterochromatin proteins (HPL-1::mKate2 and
753 HPL-2::mKate2), and Groucho homologs (TagRFP-T::LSY-22 and mNeonGreen::UNC-
754 37) in VU cells using endogenously tagged alleles. (B) Quantification of colocalization,
755 with plot reporting Manders' overlap coefficients compared to negative controls (90
756 degree rotation of one channel) and positive controls. (C) Schematic of the auxin
757 inducible degron (AID) system, where $_{At}$TIR1 mediates proteasomal degradation of AID-
758 tagged proteins in the presence of auxin. (D) Representative images of phenotypes
759 observed following individual AID-depletion of UNC-37 and LSY-22 compared to control
760 animals without AID-tagged alleles. All animals compared here are expressing TIR1
761 ubiquitously (*rpl-28p*::$_{At}$TIR1::T2A::mCherry::HIS-11) and an AC marker (*cdh-*
762 *3p*::mCherry::moeABD). Insets depict different z planes of the same image. (E)
763 Quantification of AC marker (*cdh-3p*::mCherry::moeABD) expression in ectopic ACs
764 resulting from AID-depletion of UNC-37 and LSY-22 compared to control AC and VU
765 cells.

766

767 **Figure 4–figure supplement 1: Knock-in alleles of *lsy-22*.** Schematics of the
768 new endogenously tagged loci generated in this paper for *lsy-22*. Scale bar, 100
769 base pairs (bp).

770

771 **Figure 4–figure supplement 2: UNC-37 mutants show ectopic expression of**
772 **AC markers.** Ectopic expression of AC marker (*cdh-3p*::mCherry::moeABD) in

773 hypomorphic (*unc-37(e262wd26)*) and null (*unc-37(wd17wd22)*) alleles of *unc-37*
774 compared to wild-type *unc-37*. Insets depict different z planes of the same image.
775
776 **Figure 5: POP-1 is enriched in VU cells and colocalizes with NHR-67 punctae.** (A-
777 B) Expression of mNeonGreen::UNC-37 and mNeonGreen::LSY-22 (A) and
778 eGFP::POP-1 (B) in the AC/VU precursors pre-specification (left), as well as in the AC
779 and VU cells post-specification (right). (C) Quantification of UNC-37, LSY-22, and POP-
780 1 expression at the time of AC invasion. (D) Co-visualization of NHR-67::mScarlet-I and
781 eGFP::POP-1 in the VU. (E) Quantification of POP-1 and NHR-67 colocalization, with
782 plot reporting Manders' overlap coefficient compared to negative and positive controls.
783 (F) Representative micrographs showing expression of POPTOP, a synthetic *pop-1*-
784 activated reporter construct, in wild-type ACs, VU cells, and their precursors. Insets
785 depict different z planes of the same image. (G-H) Micrographs (G) and quantification
786 (H) of eGFP-tagged POP-1 expression in proliferative ACs following RNAi depletion of
787 *nhr-67* compared to empty vector control.
788
789 **Figure 5–figure supplement 1: Expression of LSY-22, UNC-37, and POP-1**
790 **over developmental time.** (A-B) Developmental series (A) and quantified
791 expression (B) of mNeonGreen::UNC-37, mNeonGreen::LSY-22, and
792 eGFP::POP-1 expression in the AC/VU precursors, AC, and VU cells over time.
793 Following AC/VU cell specification, animals are staged by the division of the
794 underlying primary vulval precursor cells (1° VPCs).
795
796 **Figure 5–figure supplement 2: POP-1 function in VU cells is distinct from**
797 **activating role in distal somatic gonad.** (A) Schematics representing the dual
798 functions of POP-1. In the presence of Wnt signaling, POP-1 binds to its co-
799 activator β-catenin (e.g., SYS-1) and activates transcription of its target genes. In
800 the absence of Wnt signaling, POP-1 binds to its co-repressor Groucho (UNC-
801 37) and represses transcription of its target genes. (B) Representative
802 micrographs of eGFP::POP-1 and POPTOP (*pes-10*::7x-TCF::mCherry)
803 expression in the AC, dorsal uterine cells (DU), spermatheca/sheath cells (SS),

804 and VU cells. (C) Schematic of SYS-1 (β-catenin) expression in the Z1/Z4
805 lineage (based on Philips et al., 2007).
806
807 **Figure 5–figure supplement 3: POP-1 expression is regulated by the cell**
808 **cycle-dependent pro-invasion pathway.** (A-B) Representative micrographs of
809 eGFP::POP-1 and POPTOP (*pes-10*::7x-TCF::mCherry) following RNAi-induced
810 knockdown of pro-invasive transcription factors and chromatin modifiers
811 compared to control AC and VU cells. (B) Quantification of eGFP::POP-1
812 expression in ACs following RNAi treatments. Here, the presence of multiple ACs
813 are the result of failure of the AC to exit the cell cycle.
814
815 **Figure 6: Ectopic ACs arise through VU-to-AC cell fate transformation.** (A)
816 Representative images of ectopic AC (*cdh-3p*::mCherry::moeABD; LAG-
817 2::P2A::H2B::mTurquoise2) phenotypes observed following RNAi depletion of POP-1.
818 Schematics (right) depict potential explanations for observed phenotypes. (B)
819 Expression of AC markers and a VU cell marker (LAG-1::mNeonGreen, inverted to aid
820 visualization) in *pop-1(RNAi)* treated animals over time. (C) Quantification of LAG-2
821 (magenta) and LAG-1 (blue) expression in transdifferentiating cells produced by *pop-*
822 *1(RNAi)* over time.
823
824 **Figure 6–figure supplement 1: POP-1 functions to regulate AC/VU cell fates**
825 **post-specification.** (A) Schematic of the anti-GFP nanobody protein
826 degradation system (based on Wang et al., 2017). (B) Micrographs
827 demonstrating that the anti-GFP nanobody (driven under the *egl-43L* promoter) is
828 not expressed pre-specification or even shortly after when the presumptive AC
829 begins to express its differentiated cell reporter (*cdh-3*). (C) With decreased
830 levels of *pop-1*, a low penetrance (~7%) of multi-AC phenotypes were observed.
831
832 **Figure 6–figure supplement 2: Ectopic ACs resulting from *pop-1***
833 **perturbation express VU cell markers.** Expression of AC markers (*cdh-*
834 *3p*::mCherry::moeABD; LAG-2::P2A::H2B::mTurquoise2) and VU marker (LAG-

1::mNeonGreen) in *pop-1(RNAi)* treated animals compared to empty vector control.

Figure 7: NHR-67 binds to UNC-37 through IDR-mediated protein-protein interaction. (A) Predicted structure of NHR-67 generated by AlphaFold. (B) Measure of intrinsic disorder of NHR-67 using the PONDR VSL2 prediction algorithm. (C) Schematic of NHR-67 protein coding sequences used for Yeast two-hybrid experiments with reference to its intrinsically disordered region (IDR, magenta), DNA binding domain (DBD, green), and ligand binding domain (LBD, cyan). Scale bar, 10 amino acids. (D) Yeast two-hybrid experiment shows pairing of UNC-37 with either full-length NHR-67 or the IDR alone allows for yeast growth in the presence of competitive inhibitor 3-AT (20 mM). (E) Possible models of the roles of NHR-67, UNC-37, LSY-22, and POP-1 in maintenance of AC and VU cell fate. In the ventral uterine cells, the association of NHR-67 with the Groucho/TCF complex may result in repression of NHR-67 targets (top) or sequestration of NHR-67 away from its targets (bottom).

Figure 7–figure supplement 1. NHR-67 exhibits protein-protein interaction with UNC-37. Yeast two-hybrid experiment pairing UNC-37 and NHR-67 Gal4-AD prey with LSY-22, NHR-67, and POP-1 Gal4-DBD bait on SC-HIS-TRP-LEU plates with and without competitive inhibitor 3-AT (20 mM).

Source data

Figure 1–source data 1. Raw data of GFP-tagged transcription factor expression in the AC and VU cells, as reported in Figure 1C,D and Figure 1–figure supplement 1B,C. In all source files: ROI, region of interest; BG, background; BS, background-subtracted.

Figure 1–source data 2. Raw data of LAG-2::P2A::H2B::mTurquoise2 and LIN-12::mNeonGreen expression in NHR-67-deficient ACs compared to control AC and VU cells, as reported in Figure 1E and Figure 1–figure supplement 2A,B.

866 **Figure 2–source data 1.** Raw data of NHR-67::GFP expression in the AC and VU cells
867 following heat-shock inducible expression of HLH-2, as reported in Figure 2A,B.
868
869 **Figure 2–source data 2.** Raw data of GFP::HLH-2 and NHR-67::TagRFP-T expression
870 in the AC and VU cells following *uba-1* RNAi treatment compared to empty vector
871 controls, as reported in Figure 2–figure supplement 1B-D.
872
873 **Figure 3–source data 1.** Raw data of CDK sensor (DHB) ratios in VU cells over time,
874 as reported in Figure 3D,E.
875
876 **Figure 3–source data 2.** Raw data of NHR-67::GFP puncta expression following
877 photobleaching overtime, as reported in Figure 3G,H.
878
879 **Figure 4–source data 1.** Raw data of protein colocalization in VU cells, as reported in
880 Figure 4A,B and Figure 5D,E.
881
882 **Figure 4–source data 2.** Raw data of CDH-3 expression in the ectopic ACs resulting
883 from auxin-mediated depletion of AID-tagged LSY-22 or UNC-37, as reported Figure
884 4D,E.
885
886 **Figure 5–source data 1.** Raw data of mNG::UNC-37, mNG::LSY-22, and eGFP::POP-
887 1 expression in the AC/VU precursors, the AC, and VU cells, as reported in Figure 5A-C
888 and Figure 5–figure supplement 1A,B.
889
890 **Figure 5–source data 2.** Raw data of eGFP::POP-1 expression in ACs resulting from
891 RNAi knockdown of transcription factors and chromatin modifiers compared to empty
892 vector controls, reported in Figure 5F,G and Figure 5–figure supplement 2A,B.
893
894 **Figure 6–source data 1.** Raw data of LAG-2::P2A::H2B::mT2 and LAG-1::mNG
895 expression during VU-to-AC transdifferentiation, as reported in Figure 6B,C.
896

References

Adikes RC, Kohrman AQ, Martinez MAQ, Palmisano NJ, Smith JJ, Medwig-Kinney TN, Min M, Sallee MD, Ahmed OB, Kim N, Liu S, Morabito RD, Weeks N, Zhao Q, Zhang W, Feldman JL, Barkoulas M, Pani AM, Spencer SL, Martin BL, Matus DQ. 2020. Visualizing the metazoan proliferation-quiescence decision in vivo. *Elife* **9**:1–74. doi:10.7554/eLife.63265

Ashley G, Duong T, Levenson MT, Martinez MAQ, Johnsen LC, Hibshman JD, Saeger HN, Palmisano NJ, Doonan R, Martinez-Mendez R, Davidson B, Zhang W, Ragle JM, Medwig-Kinney TN, Sirota SS, Goldstein B, Matus DQ, Dickinson DJ, Reiner DJ, Ward JD. 2021. An expanded auxin-inducible degron toolkit for Caenorhabditis elegans . *Genetics*. doi:10.1093/genetics/iyab006

Attner MA, Keil W, Benavidez JM, Greenwald I. 2019. HLH-2/E2A Expression Links Stochastic and Deterministic Elements of a Cell Fate Decision during C. elegans Gonadogenesis. *Curr Biol* **29**:1–7. doi:10.1016/j.cub.2019.07.062

Bekas KN, Phillips BT. 2022. unc-37/Groucho and lsy-22/AES repress Wnt target genes in C. elegans asymmetric cell divisions. *bioRxiv*.

Benavidez JM, Kim JH, Greenwald I. 2022. Influences of HLH-2 stability on anchor cell fate specification during Caenorhabditis elegans gonadogenesis. *G3: Genes|Genomes|Genetics*.

Bodofsky S, Liberatore K, Pioppo L, Lapadula D, Thompson L, Birnbaum S, McClung G, Kartik A, Clever S, Wightman B. 2018. A tissue-specific enhancer of the C. elegans nhr-67/tailless gene drives coordinated expression in uterine stem cells and the differentiated anchor cell. *Gene Expr Patterns* **30**:71–81. doi:10.1016/j.gep.2018.10.003

Boija A, Klein IA, Sabari BR, Dall'Agnese A, Coffey EL, Zamudio A V., Li CH, Shrinivas K, Manteiga JC, Hannett NM, Abraham BJ, Afeyan LK, Guo YE, Rimel JK, Fant CB, Schuijers J, Lee TI, Taatjes DJ, Young RA. 2018. Transcription Factors Activate Genes through the Phase-Separation Capacity of Their Activation Domains. *Cell* **175**:1842-1855.e16. doi:10.1016/j.cell.2018.10.042

Bolte S, Cordelières FP. 2006. A guided tour into subcellular colocalization analysis in light microscopy. *J Microsc* **224**:213–232. doi:10.1111/j.1365-2818.2006.01706.x

Boxem M, Maliga Z, Klitgord N, Li N, Lemmens I, Mana M, de Lichtervelde L, Mul JD, van de Peut D, Devos M, Simonis N, Yildirim MA, Cokol M, Kao HL, de Smet AS, Wang H, Schlaitz AL, Hao T, Milstein S, Fan C, Tipsword M, Drew K, Galli M, Rhrissorrakrai K, Drechsel D, Koller D, Roth FP, Iakoucheva LM, Dunker AK, Bonneau R, Gunsalus KC, Hill DE, Piano F, Tavernier J, van den Heuvel S, Hyman AA, Vidal M. 2008. A Protein Domain-Based Interactome Network for C. elegans Early Embryogenesis. *Cell* **134**:534–545. doi:10.1016/j.cell.2008.07.009

Brangwynne CP, Eckmann CR, Courson DS, Rybarska A, Hoege C, Gharakhani J, Jülicher F, Hyman AA. 2009. Germline P Granules Are Liquid Droplets That Localize by Controlled Dissolution/Condensation. *Science (80-)* **324**:1729–1732.

Brenner S. 1974. The genetics of *Caenorabditis elegans*. *Genetics* **77**:71–94. doi:10.1016/S0047-2484(78)80101-8

Brumbaugh J, Stefano B Di, Hochedlinger K. 2019. Reprogramming : identifying the mechanisms that safeguard cell identity. *Development* **146**:1–17. doi:10.1242/dev.182170

943 Calvo D, Victor M, Gay F, Sui G, Po-Shan Luke M, Dufourcq P, Wen G, Maduro M,
944 Rothman J, Shi Y. 2001. A POP-1 repressor complex restricts inappropriate cell
945 type-specific gene transcription during Caenorhabditis elegans embryogenesis.
946 *EMBO J* **20**:7197–7208. doi:10.1093/emboj/20.24.7197
947 Cho WK, Spille JH, Hecht M, Lee C, Li C, Grube V, Cisse II. 2018. Mediator and RNA
948 polymerase II clusters associate in transcription-dependent condensates. *Science*
949 *(80-)* **361**:412–415. doi:10.1126/science.aar4199
950 Chong S, Dugast-Darzacq C, Liu Z, Dong P, Dailey GM, Cattoglio C, Heckert A, Banala
951 S, Lavis L, Darzacq X, Tjian R. 2018. Imaging dynamic and selective low-
952 complexity domain interactions that control gene transcription. *Science (80-)* **361**.
953 doi:10.1126/science.aar2555
954 Cohen J. 1992. A Power Primer. *Psychol Bull* **112**:155–159. doi:10.1038/141613a0
955 Davis RL, Weintraub H, Lassar AB. 1987. Expression of a single transfected cDNA
956 converts fibroblasts to myoblasts. *Cell* **51**:987–1000. doi:10.1016/0092-
957 8674(87)90585-X
958 Dickinson DJ, Goldstein B. 2016. CRISPR-based methods for caenorhabditis elegans
959 genome engineering. *Genetics* **202**:885–901. doi:10.1534/genetics.115.182162
960 Dickinson DJ, Pani AM, Heppert JK, Higgins CD, Goldstein B. 2015. Streamlined
961 genome engineering with a self-excising drug selection cassette. *Genetics*
962 **200**:1035–1049. doi:10.1534/genetics.115.178335
963 Flowers EB, Poole RJ, Tursun B, Bashllari E, Pe'er I, Hobert O. 2010. The Groucho
964 ortholog UNC-37 interacts with the short Groucho-like protein LSY-22 to control
965 developmental decisions in C. elegans. *Development* **137**:1799–1805.
966 doi:10.1242/dev.046219
967 Frøkjær-Jensen C, Davis MW, Ailion M, Jorgensen EM. 2013. Improved Mos1-mediated
968 transgenesis in C. elegans. *Nat Meth* **9**:117–118. doi:10.1038/mp.2011.182.doi
969 Fukushige T, Krause M. 2005. The myogenic potency of HLH-1 reveals wide-spread
970 developmental plasticity in early C. elegans embryos. *Development* **132**:1795–
971 1805. doi:10.1242/dev.01774
972 Ghanta KS, Mello CC. 2020. Melting dsDNA donor molecules greatly improves
973 precision genome editing in caenorhabditis elegans. *Genetics* **216**:643–650.
974 doi:10.1534/genetics.120.303564
975 Gilleard JS, McGhee JD. 2001. Activation of Hypodermal Differentiation in the
976 Caenorhabditis elegans Embryo by GATA Transcription Factors ELT-1 and ELT-3 .
977 *Mol Cell Biol* **21**:2533–2544. doi:10.1128/mcb.21.7.2533-2544.2001
978 Gómez-Saldivar G, Osuna-Luque J, Semple JI, Glauser DA, Jarriault S, Meister P.
979 2020. Tissue-Specific Transcription Footprinting Using RNA. *Genetics* **216**:931–
980 945.
981 Green JL, Inoue T, Sternberg PW. 2008. Opposing Wnt pathways orient cell polarity
982 during organogenesis. *Cell* **134**:646–656. doi:10.1016/j.cell.2008.06.026.Opposing
983 Greenwald IS, Sternberg PW, Robert Horvitz H. 1983. The lin-12 locus specifies cell
984 fates in Caenorhabditis elegans. *Cell* **34**:435–444. doi:10.1016/0092-
985 8674(83)90377-X
986 Hajduskova M, Baytek G, Kolundzic E, Gosdschan A. 2019. MRG-1 / MRG15 Is a
987 Barrier for Germ Cell to Neuron reprogramming. *Genetics* **211**:121–139.
988 Hanahan D. 2022. Hallmarks of Cancer: New Dimensions. *Cancer Discov* 31–47.

989 doi:10.1158/2159-8290.CD-21-1059
990 Hanahan D, Weinberg RA. 2000. The hallmarks of cancer. *Cell* **100**:57–70.
991 doi:10.1007/s00262-010-0968-0
992 Harris TW, Arnaboldi V, Cain S, Chan J, Chen WJ, Cho J, Davis P, Gao S, Grove CA,
993 Kishore R, Lee RYN, Muller HM, Nakamura C, Nuin P, Paulini M, Raciti D, Rodgers
994 FH, Russell M, Schindelman G, Auken K V., Wang Q, Williams G, Wright AJ, Yook
995 K, Howe KL, Schedl T, Stein L, Sternberg PW. 2020. WormBase: A Modern Model
996 Organism Information Resource. *Nucleic Acids Res* **48**:D762–D767.
997 doi:10.1093/nar/gkz920
998 Hills-Muckey K, Martinez MAQ, Stec N, Hebbar S, Saldanha J, Medwig-Kinney TN,
999 Moore FEQ, Ivanova M, Moraro A, Jordan D, Moss EG, Ercan S, Zinovyeva AY,
1000 Matus DQ, Christopher M. 2021. An engineered, orthogonal auxin
1001 analog/AtTIR1(F79G) pairing improves both specificity and efficacy of the auxin
1002 degradation system in Caenorhabditis elegans. *Genetics* iyab174.
1003 doi:https://doi.org/10.1093/genetics/iyab174
1004 Hoek KS, Eichhoff OM, Schlegel NC, Döbbeling U, Kobert N, Schaerer L, Hemmi S,
1005 Dummer R. 2008. In vivo switching of human melanoma cells between proliferative
1006 and invasive states. *Cancer Res* **68**:650–656. doi:10.1158/0008-5472.CAN-07-
1007 2491
1008 Horner MA, Quintin S, Domeier ME, Kimble J, Labouesse M, Mango SE. 1998. pha-4,
1009 an HNF-3 homolog, specifies pharyngeal organ identity in Caenorhabditis elegans.
1010 *Genes Dev* **12**:1947–1952. doi:10.1101/gad.12.13.1947
1011 Huang G, Jesus B De, Koh A, Blanco S, Rettmann A, Demott E, Sylvester M, Meng C,
1012 Waterland S, Rhodes A, Alicea P, Flynn A, Dickinson DJ. 2021. Improved CRISPR
1013 / Cas9 knock-in efficiency via the self-excising cassette (SEC) selection method in
1014 C . elegans. *Micropublication Biol*.
1015 Irgen-Gioro S, Yoshida S, Walling V, Chong S. 2022. Fixation can change the
1016 appearance of phase separation in living cells. *Elife* **11**. doi:10.7554/eLife.79903
1017 Jarriault S, Schwab Y, Greenwald I. 2008. A Caenorhabditis elegans model for
1018 epithelial-neuronal transdifferentiation. *Proc Natl Acad Sci* **105**:3790–3795.
1019 doi:10.1073/pnas.0712159105
1020 Jiang H, Xu Z, Zhong P, Ren Y, Liang G, Schilling HA, Hu Z, Zhang Y, Wang X, Chen
1021 S, Yan Z, Feng J. 2015. Cell cycle and p53 gate the direct conversion of human
1022 fibroblasts to dopaminergic neurons. *Nat Commun* **6**. doi:10.1038/ncomms10100
1023 Jin Y, Hoskins R, Horvitz HR. 1994. Control of type-D GABAergic neuron differentiation
1024 by C. elegans UNC-30 homeodomain protein. *Nature* **372**:780–783.
1025 doi:10.1038/372780a0
1026 Jumper J, Evans R, Pritzel A, Green T, Figurnov M, Ronneberger O, Tunyasuvunakool
1027 K, Bates R, Žídek A, Potapenko A, Bridgland A, Meyer C, Kohl SAA, Ballard AJ,
1028 Cowie A, Romera-Paredes B, Nikolov S, Jain R, Adler J, Back T, Petersen S,
1029 Reiman D, Clancy E, Zielinski M, Steinegger M, Pacholska M, Berghammer T,
1030 Bodenstein S, Silver D, Vinyals O, Senior AW, Kavukcuoglu K, Kohli P, Hassabis
1031 D. 2021. Highly accurate protein structure prediction with AlphaFold. *Nature*
1032 **596**:583–589. doi:10.1038/s41586-021-03819-2
1033 Kagias K, Ahier A, Fischer N, Jarriault S. 2012. Members of the NODE (Nanog and
1034 Oct4-associated deacetylase) complex and SOX-2 promote the initiation of a

1035 natural cellular reprogramming event in vivo. *Proc Natl Acad Sci U S A* **109**:6596–
1036 6601. doi:10.1073/pnas.1117031109
1037 Karp X, Greenwald I. 2003. Post-transcriptional regulation of the E/Daughterless
1038 ortholog HLH-2, negative feedback, and birth order bias during the AC/VU decision
1039 in C. elegans. *Genes Dev* **17**:3100–3111. doi:10.1101/gad.1160803
1040 Katsanos D, Barkoulas M. 2022. Targeted DamID in C . elegans reveals a direct role for
1041 LIN-22 and NHR-25 in antagonizing the epidermal stem cell fate. *Sci Adv*
1042 **8**:eabk3141.
1043 Keeley DP, Hastie E, Jayadev R, Kelley LC, Chi Q, Payne SG, Jeger JL, Hoffman BD,
1044 Sherwood DR. 2020. Comprehensive Endogenous Tagging of Basement
1045 Membrane Components Reveals Dynamic Movement within the Matrix Scaffolding.
1046 *Dev Cell* **54**:60-74.e7. doi:10.1016/j.devcel.2020.05.022
1047 Kelley LC, Wang Z, Hagedorn EJ, Wang L, Shen W, Lei S, Johnson SA, Sherwood DR.
1048 2017. Live-cell confocal microscopy and quantitative 4D image analysis of anchor-
1049 cell invasion through the basement membrane in Caenorhabditis elegans. *Nat*
1050 *Protoc* **12**:2081–2096. doi:10.1038/nprot.2017.093
1051 Kiefer JC, Smith PA, Mango SE. 2007. PHA-4/FoxA cooperates with TAM-1/TRIM to
1052 regulate cell fate restriction in the C. elegans foregut. *Dev Biol* **303**:611–624.
1053 doi:10.1016/j.ydbio.2006.11.042
1054 Kimble J, Hirsh D. 1979. The postembryonic cell lineages of the hermaphrodite and
1055 male gonads in Caenorhabditis elegans. *Dev Biol* **70**:396–417. doi:10.1016/0012-
1056 1606(79)90035-6
1057 Kohrman AQ, Matus DQ. 2017. Divide or Conquer: Cell Cycle Regulation of Invasive
1058 Behavior. *Trends Cell Biol*. doi:10.1016/j.tcb.2016.08.003
1059 Kolundzic E, Ofenbauer A, Bulut SI, Uyar B, Baytek G, Sommermeier A, Seelk S, He M,
1060 Hirsekorn A, Vucicevic D, Akalin A, Diecke S, Lacadie SA, Tursun B. 2018. FACT
1061 Sets a Barrier for Cell Fate Reprogramming in Caenorhabditis elegans and Human
1062 Cells. *Dev Cell* **46**:611-626.e12. doi:10.1016/j.devcel.2018.07.006
1063 Kurashina M, Wang J, Lin J, Lee KK, Johal A, Mizumoto K. 2021. Sustained expression
1064 of unc-4 homeobox gene and unc-37/groucho in postmitotic neurons specifies the
1065 spatial organization of the cholinergic synapses in c. Elegans. *Elife* **10**:1–26.
1066 doi:10.7554/eLife.66011
1067 Larson AG, Elnatan D, Keenen MM, Trnka MJ, Johnston JB, Burlingame AL, Agard DA,
1068 Redding S, Narlikar GJ. 2017. Liquid droplet formation by HP1α suggests a role for
1069 phase separation in heterochromatin. *Nature* **547**:236–240.
1070 doi:10.1038/nature22822
1071 Leyva-Díaz E, Hobert O. 2019. Transcription factor autoregulation is required for
1072 acquisition and maintenance of neuronal identity. *Development* **146**.
1073 doi:10.1242/dev.177378
1074 Li S, Armstrong CM, Bertin N, Ge H, Milstein S, Boxem M, Vidalain PO, Han JDJ,
1075 Chesneau A, Hao T, Goldberg DS, Li N, Martinez M, Rual JF, Lamesch P, Xu L,
1076 Tewari M, Wong SL, Zhang L V., Berriz GF, Jacotot L, Vaglio P, Reboul J,
1077 Hirozane-Kishikawa T, Li Q, Gabel HW, Elewa A, Baumgartner B, Rose DJ, Yu H,
1078 Bosak S, Sequerra R, Fraser A, Mango SE, Saxton WM, Strome S, Van Den
1079 Heuvel S v., Piano F, Vandenhaute J, Sardet C, Gerstein M, Doucette-Stamm L,
1080 Gunsalus KC, Harper JW, Cusick ME, Roth FP, Hill DE, Vidal M. 2004. A Map of

1081 the Interactome Network of the Metazoan C. elegans. *Science (80-)* **303**:540–543.
1082 doi:10.1126/science.1091403
1083 Liang B, Wang J. 2020. EVI1 in leukemia and solid tumors. *Cancers (Basel)* **12**:1–17.
1084 doi:10.3390/cancers12092667
1085 Lim B, Levine MS. 2021. Enhancer-promoter communication: hubs or loops? *Curr Opin*
1086 *Genet Dev* **67**:5–9. doi:10.1016/j.gde.2020.10.001
1087 Ma X, Zhao Z, Xiao L, Xu W, Kou Y, Zhang Y, Wu G, Wang Y, Du Z. 2021. A 4D single-
1088 cell protein atlas of transcription factors delineates spatiotemporal patterning during
1089 embryogenesis. *Nat Methods* **18**:893–902. doi:10.1038/s41592-021-01216-1
1090 Maduro MF, Lin R, Rothman JH. 2002. Dynamics of a developmental switch: Recursive
1091 intracellular and intranuclear redistribution of Caenorhabditis elegans POP-1
1092 parallels Wnt-inhibited transcriptional repression. *Dev Biol* **248**:128–142.
1093 doi:10.1006/dbio.2002.0721
1094 Martinez M, Matus D. 2020. Auxin-mediated Protein Degradation in Caenorhabditis
1095 elegans. *Bio-Protocol* **10**:1–13. doi:10.21769/bioprotoc.3589
1096 Martinez MAQ, Kinney BA, Medwig-Kinney TN, Ashley G, Ragle JM, Johnson L,
1097 Aguilera J, Hammell CM, Ward JD, Matus DQ. 2020. Rapid Degradation of
1098 Caenorhabditis elegans Proteins at Single-Cell Resolution with a Synthetic Auxin.
1099 *G3 Genes, Genomes, Genet* **10**:267–280. doi:10.1534/g3.119.400781
1100 Matus DQ, Li X-Y, Durbin S, Agarwal D, Chi Q, Weiss SJ, Sherwood DR. 2010. In vivo
1101 identification of regulators of cell invasion across basement membranes. *Sci Signal*
1102 **3**:ra35. doi:10.1126/scisignal.2000654
1103 Matus DQ, Lohmer LL, Kelley LC, Schindler AJ, Kohrman AQ, Barkoulas M, Zhang W,
1104 Chi Q, Sherwood DR. 2015. Invasive Cell Fate Requires G1 Cell-Cycle Arrest and
1105 Histone Deacetylase-Mediated Changes in Gene Expression. *Dev Cell* **35**:162–
1106 174. doi:10.1016/j.devcel.2015.10.002
1107 McKim KS, Peters K, Rose AM. 1993. Two Types of Sites Required for Meiotic
1108 Chromosome Pairing in Caenorhabditis elegans. *Genetics* **134**:749–768.
1109 Medwig-Kinney TN, Palmisano NJ, Matus DQ. 2021. Deletion of a putative HDA-1
1110 binding site in the hlh-2 promoter eliminates expression in C. elegans dorsal uterine
1111 cells. *Micropublication Biol* **1**.
1112 Medwig-Kinney TN, Sirota SS, Gibney T V., Pani AM, Matus DQ. 2022. An in vivo
1113 toolkit to visualize endogenous LAG-2/Delta and LIN-12/Notch signaling in C.
1114 elegans. *microPublication Biol*.
1115 Medwig-Kinney TN, Smith JJ, Palmisano NJ, Tank S, Zhang W, Matus DQ. 2020. A
1116 developmental gene regulatory network for C. elegans anchor cell invasion.
1117 *Development* **147**:dev185850. doi:https://doi.org/10.1101/691337
1118 Medwig TN, Matus DQ. 2017. Breaking down barriers: the evolution of cell invasion.
1119 *Curr Opin Genet Dev* **47**:33–40. doi:10.1016/j.gde.2017.08.003
1120 Milde-Langosch K. 2005. The Fos family of transcription factors and their role in
1121 tumourigenesis. *Eur J Cancer* **41**:2449–2461. doi:10.1016/j.ejca.2005.08.008
1122 Mondal C, Gacha-Garay MJ, Larkin K, Adikes R, Di Martino J, Chien C-C, Fraser M,
1123 Eni-aganga I, Agullo-Pascual E, Ozbek U, Naba A, Gaitas A, Fu T-M, Upadhyayula
1124 S, Betzig E, Matus D, Martin BL, Bravo-Cordero JJ. 2021. A Proliferative to
1125 Invasive Switch is Mediated by srGAP1 Downregulation Through the Activation of
1126 TGFβ2 Signaling. *SSRN Electron J* **40**:111358.

doi:https://doi.org/10.1016/j.celrep.2022.111358 ll
Nelson AT, Wang Y, Nelson ER. 2021. TLX, an Orphan Nuclear Receptor with Emerging Roles in Physiology and Disease. *Endocrinol (United States)* **162**:1–13. doi:10.1210/endocr/bqab184
Pani AM, Gibney T V., Medwig-Kinney TN, Matus DQ, Goldstein B. 2022. A new toolkit to visualize and perturb endogenous LIN-12/Notch signaling. *Micropublication Biol*.
Patel T, Hobert O. 2017. Coordinated control of terminal differentiation and restriction of cellular plasticity. *Elife* **6**:1–26. doi:10.7554/elife.24100
Patel T, Tursun B, Rahe DP, Hobert O. 2012. Removal of Polycomb Repressive Complex 2 Makes C. elegans Germ Cells Susceptible to Direct Conversion into Specific Somatic Cell Types. *Cell Rep* **2**:1178–1186. doi:10.1016/j.celrep.2012.09.020
Peng QY, Zhang QF. 2006. Precise positions of Phoebe determined with CCD image-overlapping calibration. *Mon Not R Astron Soc* **366**:208–212. doi:10.1186/1471-2105-7-208
Pflugrad A, Meir JYJ, Barnes TM, Miller DM. 1997. The Groucho-like transcription factor UNC-37 functions with the neural specificity gene unc-4 to govern motor neuron identity in C. elegans. *Development* **124**:1699–1709. doi:10.1242/dev.124.9.1699
Phillips BT, Kidd AR, King R, Hardin J, Kimble J. 2007. Reciprocal asymmetry of SYS-1/β-catenin and POP-1/TCF controls asymmetric divisions in Caenorhabditis elegans. *Proc Natl Acad Sci U S A* **104**:3231–3236. doi:10.1073/pnas.0611507104
Phillips BT, Kimble J. 2009. A New Look at TCF and β-Catenin through the Lens of a Divergent C. elegans Wnt Pathway. *Dev Cell* **17**:27–34. doi:10.1016/j.devcel.2009.07.002
Porta-de-la-Riva M, Fontrodona L, Villanueva A, Cerón J. 2012. Basic Caenorhabditis elegans Methods: Synchronization and Observation. *J Vis Exp* 1–9. doi:10.3791/4019
Putnam A, Cassani M, Smith J, Seydoux G. 2019. A gel phase promotes condensation of liquid P granules in Caenorhabditis elegans embryos. *Nat Struct Mol Biol* **26**.
Quintin S, Michaux G, McMahon L, Gansmuller A, Labouesse M. 2001. The Caenorhabditis elegans gene lin-26 can trigger epithelial differentiation without conferring tissue specificity. *Dev Biol* **235**:410–421. doi:10.1006/dbio.2001.0294
Rahe DP, Hobert O. 2019. Restriction of Cellular Plasticity of Differentiated Cells Mediated by Chromatin Modifiers, Transcription Factors and Protein Kinases. *G3: Genes|Genomes|Genetics* **9**:2287–2302. doi:10.1534/g3.119.400328
Reece-Hoyes JS, Deplancke B, Shingles J, Grove CA, Hope IA, Walhout AJM. 2005. A compendium of Caenorhabditis elegans regulatory transcription factors: A resource for mapping transcription regulatory networks. *Genome Biol* **6**. doi:10.1186/gb-2005-6-13-r110
Reece-Hoyes JS, Walhout AJM. 2018. High-efficiency yeast transformation. *Cold Spring Harb Protoc* **2018**:563–568. doi:10.1101/pdb.prot094995
Richard JP, Zuryn S, Fischer N, Pavet V, Vaucamps N, Jarriault S. 2011. Direct in vivo cellular reprogramming involves transition through discrete, non-pluripotent steps. *J Cell Sci* **124**:e1–e1. doi:10.1242/jcs.090043
Riddle MR, Spickard EA, Jevince A, Nguyen KCQ, Hall DH, Joshi PM, Rothman JH.

1173 2016. Transorganogenesis and transdifferentiation in C. elegans are dependent on
1174 differentiated cell identity. *Dev Biol* **420**:136–147. doi:10.1016/j.ydbio.2016.09.020
1175 Riddle MR, Weintraub A, Nguyen KCQ, Hall DH, Rothman JH. 2013.
1176 Transdifferentiation and remodeling of post-embryonic C. elegans cells by a single
1177 transcription factor. *Development* **140**:4844–4849. doi:10.1242/dev.103010
1178 Riva C, Hajduskova M, Gally C, Suman SK, Ahier A, Jarriault S. 2022. A natural
1179 transdifferentiation event involving mitosis is empowered by integrating signaling
1180 inputs with conserved plasticity factors. *Cell Rep* **40**:111365.
1181 doi:10.1016/j.celrep.2022.111365
1182 Rothman J, Jarriault S. 2019. Developmental Plasticity and Cellular Reprogramming.
1183 *Genetics* **213**:723–757.
1184 Rual JF, Ceron J, Koreth J, Hao T, Nicot AS, Hirozane-Kishikawa T, Vandenhaute J,
1185 Orkin SH, Hill DE, van den Heuvel S, Vidal M. 2004. Toward improving
1186 Caenorhabditis elegans phenome mapping with an ORFeome-based RNAi library.
1187 *Genome Res* **14**:2162–2168. doi:10.1101/gr.2505604
1188 Sabari BR, Dall'Agnese A, Boija A, Klein IA, Coffey EL, Shrinivas K, Abraham BJ,
1189 Hannett NM, Zamudio A V., Manteiga JC, Li CH, Guo YE, Day DS, Schuijers J,
1190 Vasile E, Malik S, Hnisz D, Lee TI, Cisse II, Roeder RG, Sharp PA, Chakraborty
1191 AK, Young RA. 2018. Coactivator condensation at super-enhancers links phase
1192 separation and gene control. *Science (80-)* **361**. doi:10.1126/science.aar3958
1193 Sallee MD, Aydin T, Greenwald I. 2015. Influences of LIN-12/Notch and POP-1/TCF on
1194 the Robustness of Ventral Uterine Cell Fate Specification in Caenorhabditis
1195 elegans Gonadogenesis. *G3: Genes|Genomes|Genetics* **5**:2775–2782.
1196 doi:10.1534/g3.115.022608
1197 Sallee MD, Greenwald I. 2015. Dimerization-driven degradation of C. elegans and
1198 human E proteins. *Genes Dev* **29**:1356–1361. doi:10.1101/gad.261917.115
1199 Sallee MD, Littleford HE, Greenwald I. 2017. A bHLH Code for Sexually Dimorphic
1200 Form and Function of the C. elegans Somatic Gonad. *Curr Biol* **27**:1853-1860.e5.
1201 doi:10.1016/j.cub.2017.05.059
1202 Schindelin J, Arganda-Carreras I, Frise E, Kaynig V, Longair M, Pietzsch T, Preibisch S,
1203 Rueden C, Saalfeld S, Schmid B, Tinevez J-Y, White DJ, Hartenstein V, Eliceiri K,
1204 Tomancak P, Cardona A. 2012. Fiji: an open-source platform for biological-image
1205 analysis. *Nat Methods* **9**:676–82. doi:10.1038/nmeth.2019
1206 Seydoux G, Greenwald I. 1989. Cell autonomy of lin-12 function in a cell fate decision in
1207 C. elegans. *Cell* **57**:1237–1245. doi:10.1016/0092-8674(89)90060-3
1208 Seydoux G, Schedl T, Greenwald I. 1990. Cell-cell interactions prevent a potential
1209 inductive interaction between soma and germline in C. elegans. *Cell* **61**:939–951.
1210 doi:10.1016/0092-8674(90)90060-R
1211 Sherwood DR, Sternberg PW. 2003. Anchor cell invasion into the vulval epithelium in C.
1212 elegans. *Dev Cell* **5**:21–31. doi:10.1016/S1534-5807(03)00168-0
1213 Shetty P, Lo MC, Robertson SM, Lin R. 2005. C. elegans TCF protein, POP-1, converts
1214 from repressor to activator as a result of Wnt-induced lowering of nuclear levels.
1215 *Dev Biol* **285**:584–592. doi:10.1016/j.ydbio.2005.07.008
1216 Siegfried K, Kimble J. 2002. POP-1 controls axis formation during early gonadogenesis
1217 in C. elegans. *Development* **453**:443–453.
1218 Siegfried KR, Kidd AR, Chesney MA, Kimble J. 2004. The sys-1 and sys-3 Genes

1219 Cooperate with Wnt Signaling to Establish the Proximal-Distal Axis of the
1220 Caenorhabditis elegans Gonad. *Genetics* **166**:171–186.
1221 doi:10.1534/genetics.166.1.171
1222 Simonis N, Rual JF, Carvunis AR, Tasan M, Lemmens I, Hirozane-Kishikawa T, Hao T,
1223 Sahalie JM, Venkatesan K, Gebreab F, Cevik S, Klitgord N, Fan C, Braun P, Li N,
1224 Ayivi-Guedehoussou N, Dann E, Bertin N, Szeto D, Dricot A, Yildirim MA, Lin C, de
1225 Smet AS, Kao HL, Simon C, Smolyar A, Ahn JS, Tewari M, Boxem M, Milstein S,
1226 Yu H, Dreze M, Vandenhaute J, Gunsalus KC, Cusick ME, Hill DE, Tavernier J,
1227 Roth FP, Vidal M. 2009. Empirically controlled mapping of the Caenorhabditis
1228 elegans protein-protein interactome network. *Nat Methods* **6**:47–54.
1229 doi:10.1038/nmeth.1279
1230 Smith JJ, Xiao Y, Parsan N, Medwig-Kinney TN, Martinez MAQ, Moore FEQ, Palmisano
1231 NJ, Kohrman AQ, Chandhok Delos Reyes M, Adikes RC, Liu S, Bracht SA, Zhang
1232 W, Wen K, Kratsios P, Matus DQ. 2022. The SWI/SNF chromatin remodeling
1233 assemblies BAF and PBAF differentially regulate cell cycle exit and cellular
1234 invasion in vivo, PLOS Genetics. doi:10.1371/journal.pgen.1009981
1235 Spencer SL, Cappell SD, Tsai FC, Overton KW, Wang CL, Meyer T. 2013. The
1236 proliferation-quiescence decision is controlled by a bifurcation in CDK2 activity at
1237 mitotic exit. *Cell* **155**:369–383. doi:10.1016/j.cell.2013.08.062
1238 Strom AR, Emelyanov A V., Mir M, Fyodorov D V., Darzacq X, Karpen GH. 2017. Phase
1239 separation drives heterochromatin domain formation. *Nature* **547**:241–245.
1240 doi:10.1038/nature22989
1241 Sturm Á, Saskoi É, Tibor K, Weinhardt N, Vellai T. 2018. Highly efficient RNAi and
1242 Cas9-based auto-cloning systems for C. elegans research. *Nucleic Acids Res*
1243 **46**:e105. doi:10.1093/nar/gky516
1244 Sulston JE, Horvitz HR. 1977. Post-embryonic cell lineages of the nematode,
1245 Caenorhabditis elegans. *Dev Biol* **56**:110–156. doi:10.1016/0012-1606(77)90158-0
1246 Treen N, Shimobayashi SF, Eeftens J, Brangwynne CP, Levine M. 2021. Properties of
1247 repression condensates in living Ciona embryos. *Nat Commun* **12**:1–9.
1248 doi:10.1038/s41467-021-21606-5
1249 Tursun B, Patel T, Kratsios P, Hobert O. 2011. Direct Conversion of C. elegans Germ
1250 Cells into Specific Neuron Types. *Science (80-)* **331**:304–309.
1251 van der Horst SEM, Cravo J, Woollard A, Teapal J, Van den Heuvel S. 2019. C .
1252 elegans Runx / CBFβ suppresses POP-1 (TCF) to convert asymmetric to
1253 proliferative division of stem cell-like seam cells. *Development* **146**:1–34.
1254 doi:10.1242/dev.180034
1255 Varadi M, Anyango S, Deshpande M, Nair S, Natassia C, Yordanova G, Yuan D, Stroe
1256 O, Wood G, Laydon A, Žídek A, Green T, Tunyasuvunakool K, Petersen S, Jumper
1257 J, Clancy E, Green R, Vora A, Lutfi M, Figurnov M, Cowie A, Hobbs N, Kohli P,
1258 Kleywegt G, Birney E, Hassabis D, Velankar S. 2022. AlphaFold Protein Structure
1259 Database: massively expanding the structural coverage of protein-sequence space
1260 with high-accuracy models. *Nucleic Acids Res* **50**:D439–D444.
1261 doi:10.1093/nar/gkab1061
1262 Verghese E, Schocken J, Jacob S, Wimer AM, Royce R, Nesmith JE, Baer GM, Clever
1263 S, McCain E, Lakowski B, Wightman B. 2011. The tailless ortholog nhr-67 functions
1264 in the development of the C. elegans ventral uterus. *Dev Biol* **356**:516–528.

1265 doi:10.1016/j.ydbio.2011.06.007
1266 Wang LH, Baker NE. 2015. E Proteins and ID Proteins: Helix-Loop-Helix Partners in
1267 Development and Disease. *Dev Cell* **35**:269–280. doi:10.1016/j.devcel.2015.10.019
1268 Wang S, Tang NH, Lara-Gonzalez P, Zhao Z, Cheerambathur DK, Prevo B, Chisholm
1269 AD, Desai A, Oegema K. 2017. A toolkit for GFP-mediated tissue-specific protein
1270 degradation in C. elegans. *Development* **144**:2694–2701. doi:10.1242/dev.150094
1271 Wickham H. 2016. ggplot2: Elegant Graphics for Data Analysis. Springer-Verlag New
1272 York.
1273 Wilkinson HA, Fitzgerald K, Greenwald I. 1994. Reciprocal changes in expression of the
1274 receptor lin-12 and its ligand lag-2 prior to commitment in a C. elegans cell fate
1275 decision. *Cell* **79**:1187–1198. doi:10.1016/0092-8674(94)90010-8
1276 Zacharias AL, Walton T, Preston E, Murray JI. 2015. Quantitative Differences in Nuclear
1277 β-catenin and TCF Pattern Embryonic Cells in C. elegans. *PLoS Genet* **11**.
1278 doi:10.1371/journal.pgen.1005585
1279 Zhang L, Ward JD, Cheng Z, Dernburg AF. 2015. The auxin-inducible degradation (AID)
1280 system enables versatile conditional protein depletion in C. elegans. *Development*
1281 **142**:4374–4384. doi:10.1242/dev.129635
1282 Zhong W, Sternberg PW. 2006. Genome-Wide Prediction of C. elegans Genetic
1283 Interactions. *Science (80-)* **311**:1481–1484.
1284 Zhu J, Fukushige T, McGhee JD, Rothman JH. 1998. Reprogramming of early
1285 embryonic blastomeres into endodermal progenitors by a Caenorhabditis elegans
1286 GATA factor. *Genes Dev* **12**:3809–3814. doi:10.1101/gad.12.24.3809
1287 Zuryn S, Ahier A, Portoso M, White ER, Morin MC, Margueron R, Jarriault S. 2014.
1288 Sequential histone-modifying activities determine the robustness of
1289 transdifferentiation. *Science (80-)* **345**:826–829. doi:10.1126/science.1255885
1290

Figure 1 Medwig-Kinney et al. (2023)

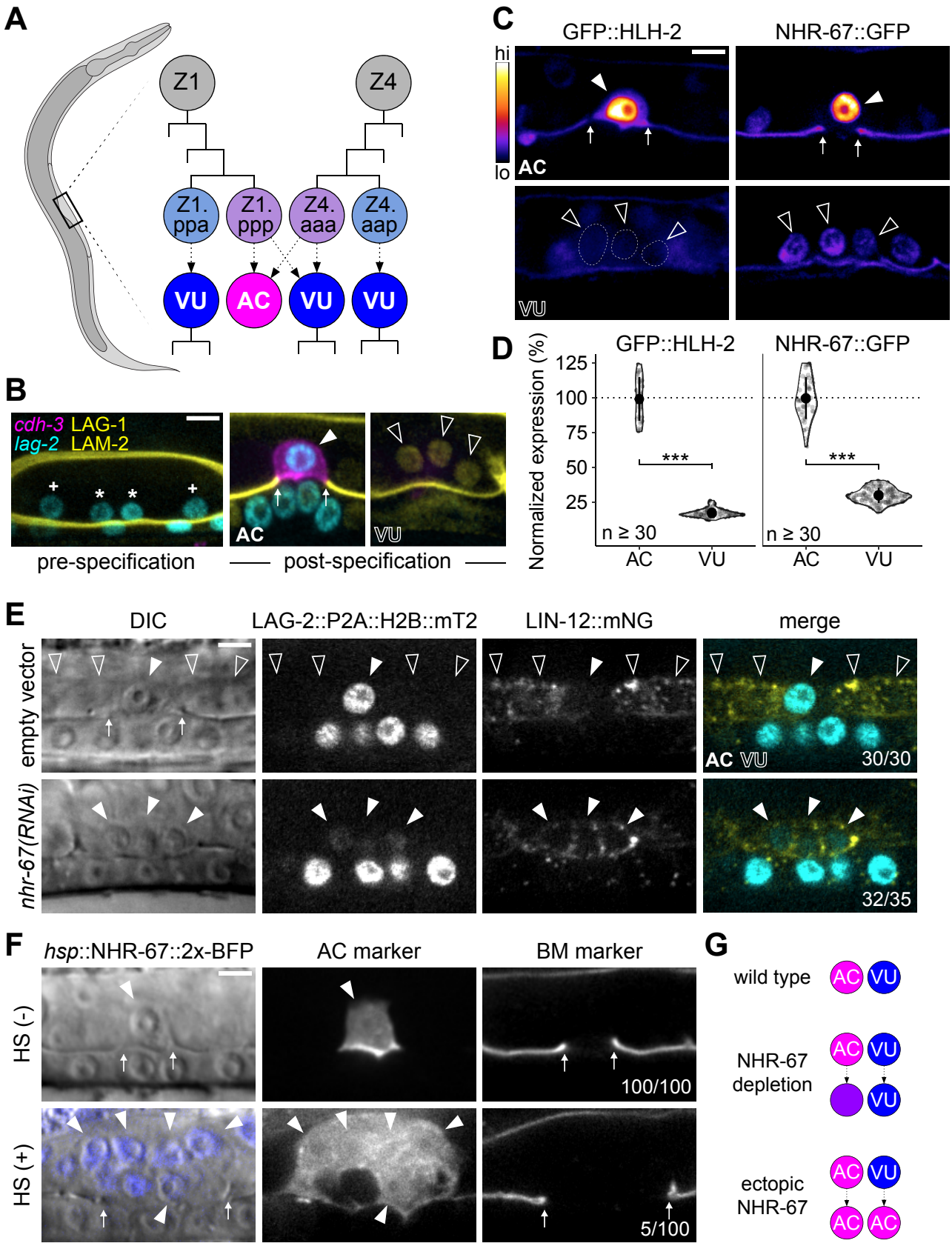

Figure 1–figure supplement 1 Medwig-Kinney et al. (2023)

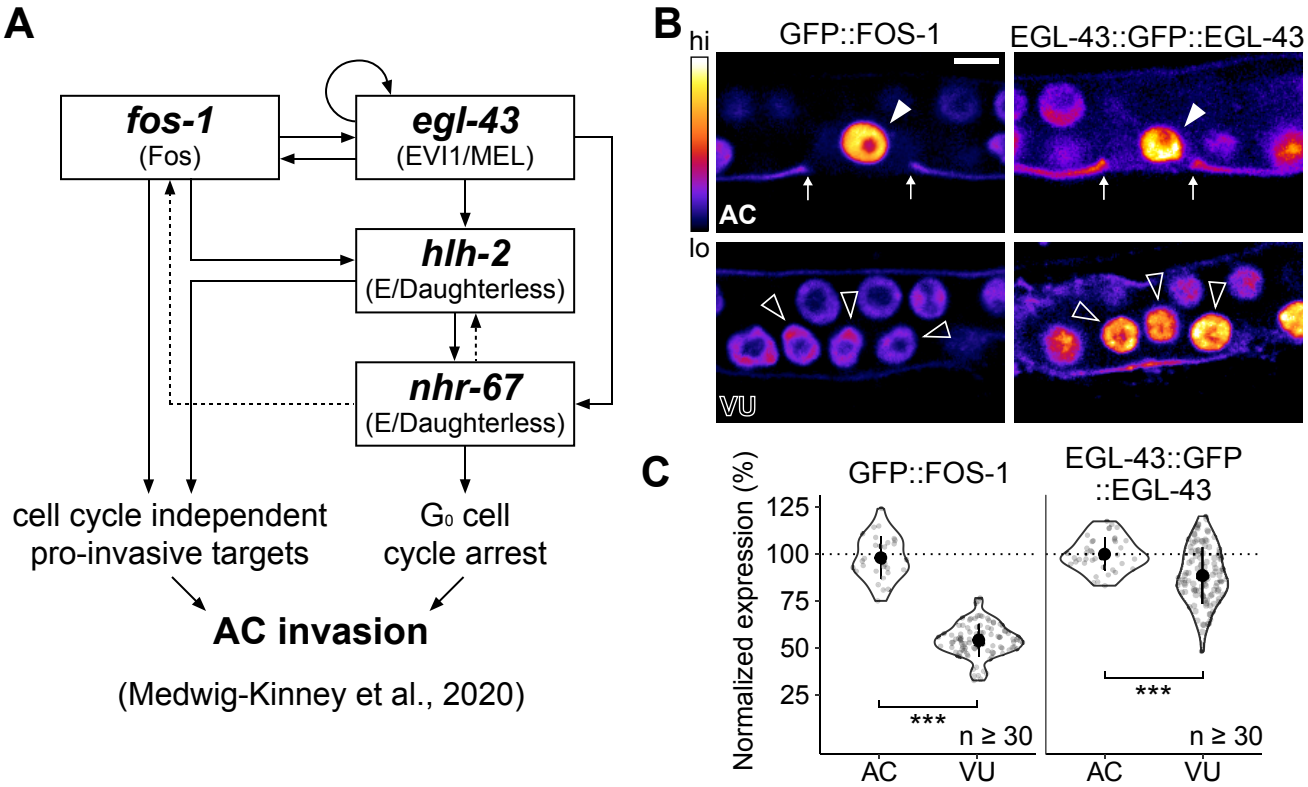

Figure 1–figure supplement 2 Medwig-Kinney et al. (2023)

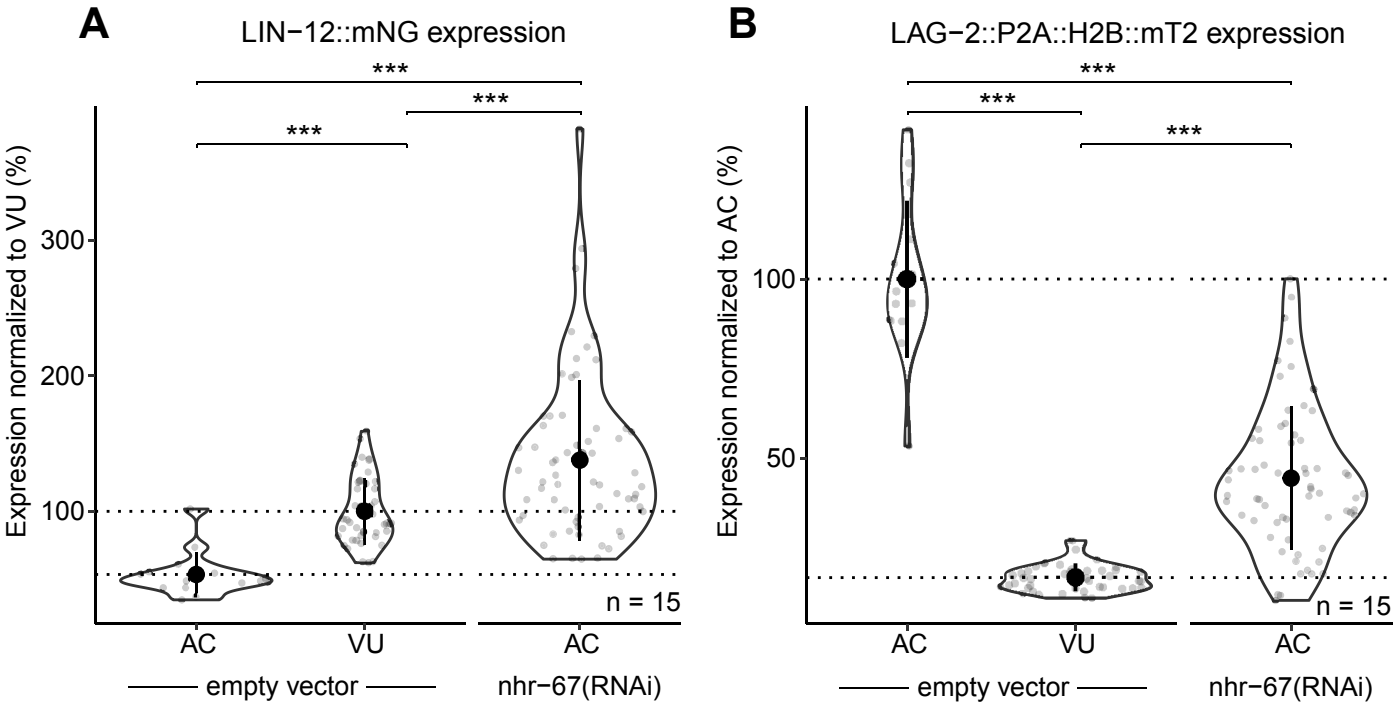

Figure 2 Medwig-Kinney et al. (2023)

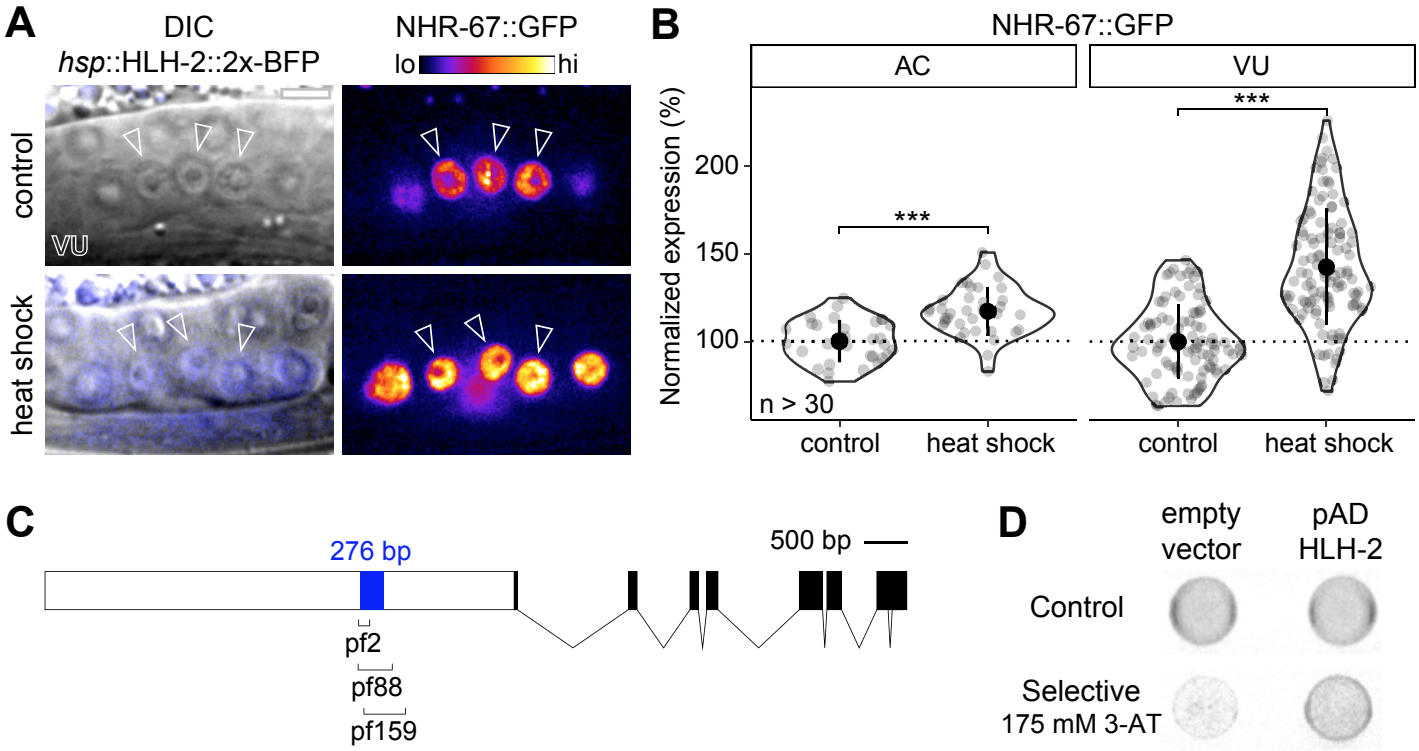

Figure 2–figure supplement 1

Medwig-Kinney et al. (2023)

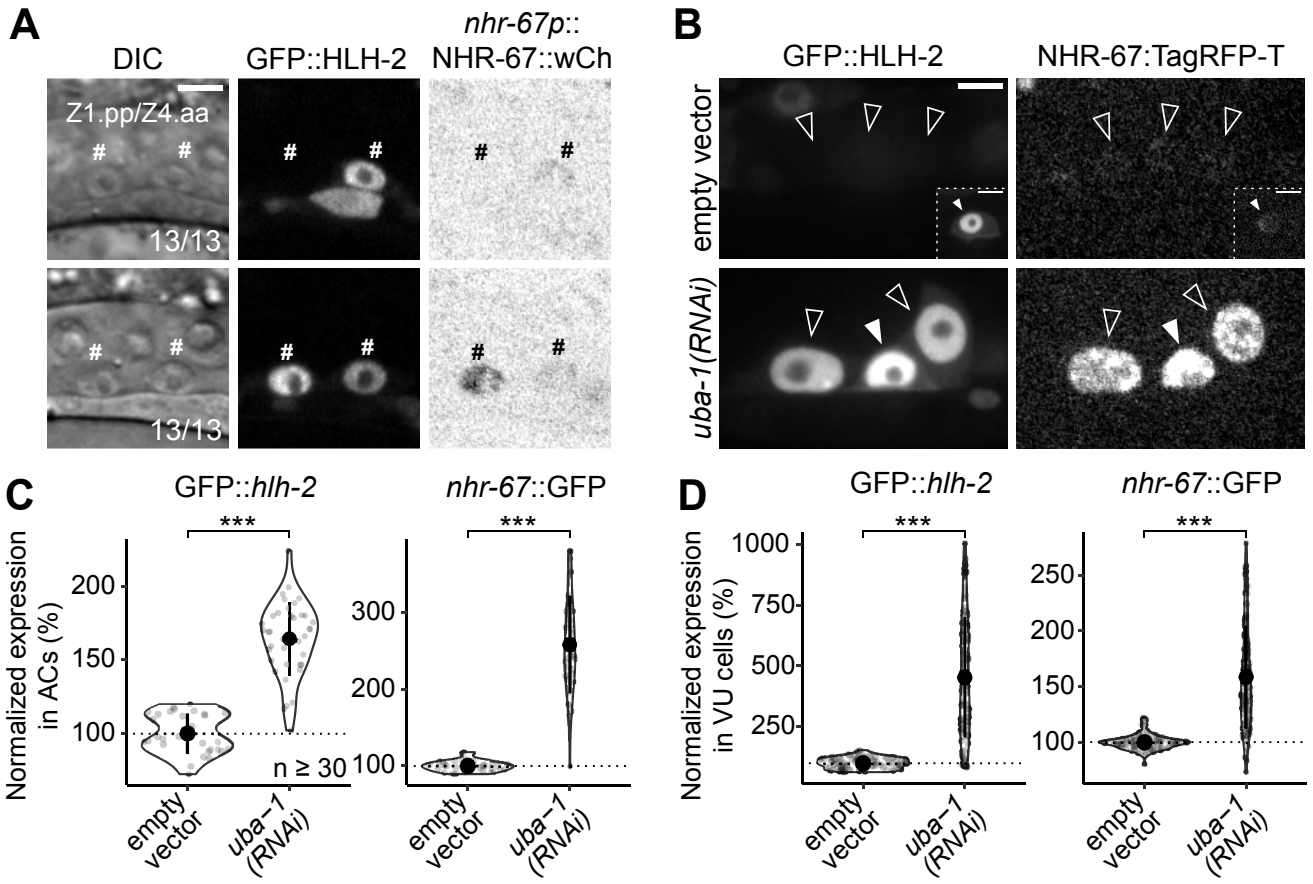

Figure 3

Medwig-Kinney et al. (2023)

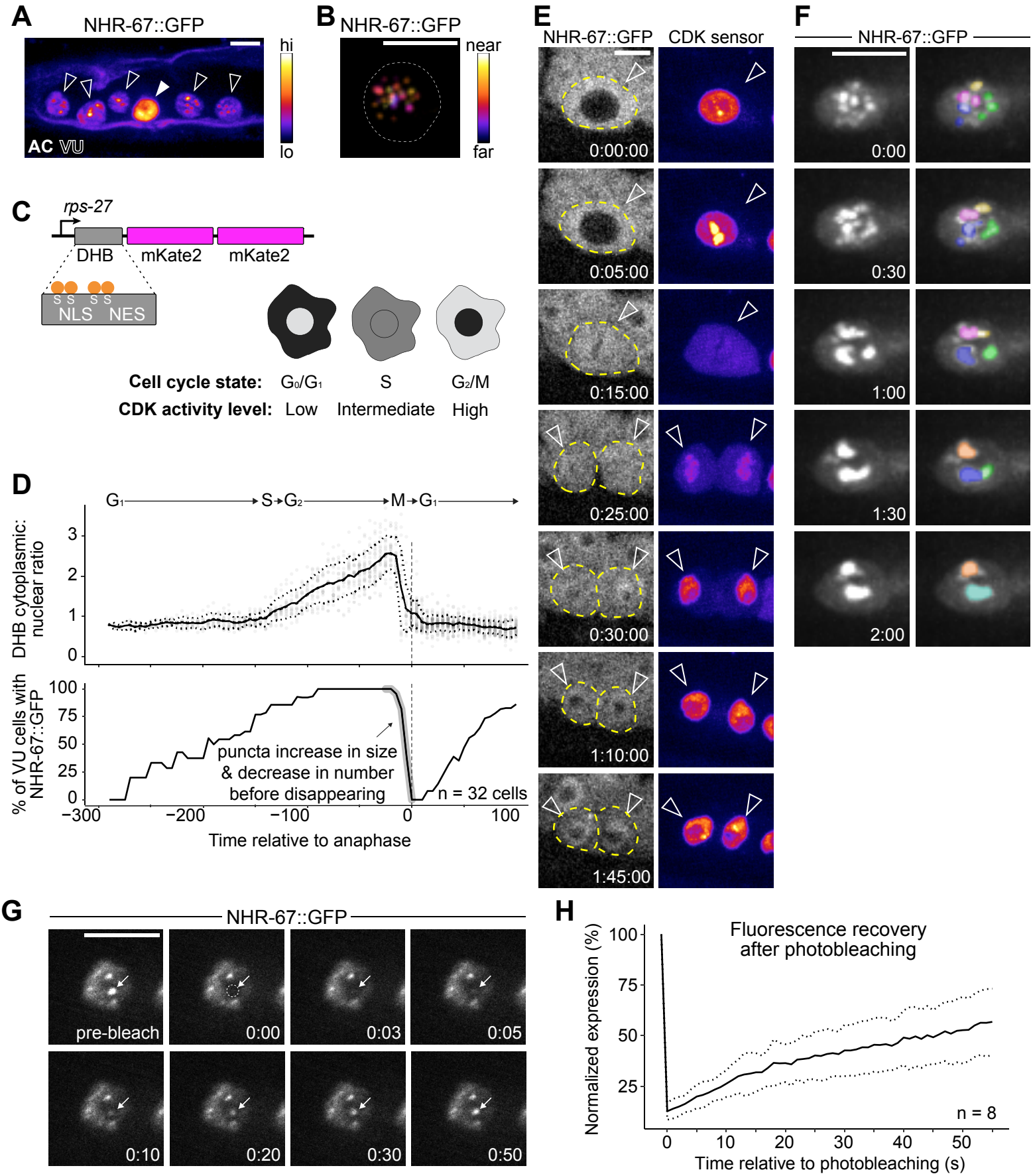

Figure 3–figure supplement 1 Medwig-Kinney et al. (2023)

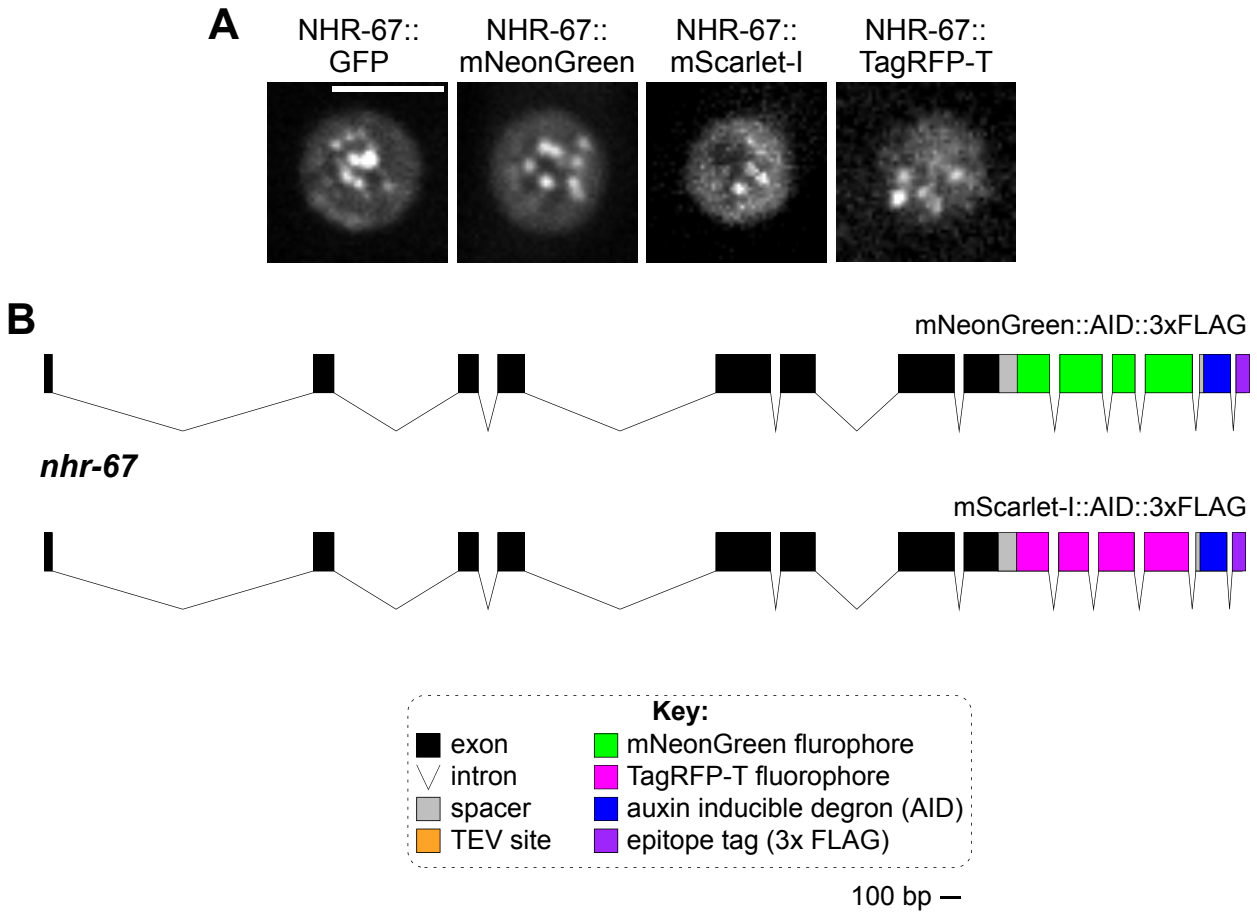

Figure 4 Medwig-Kinney et al. (2023)

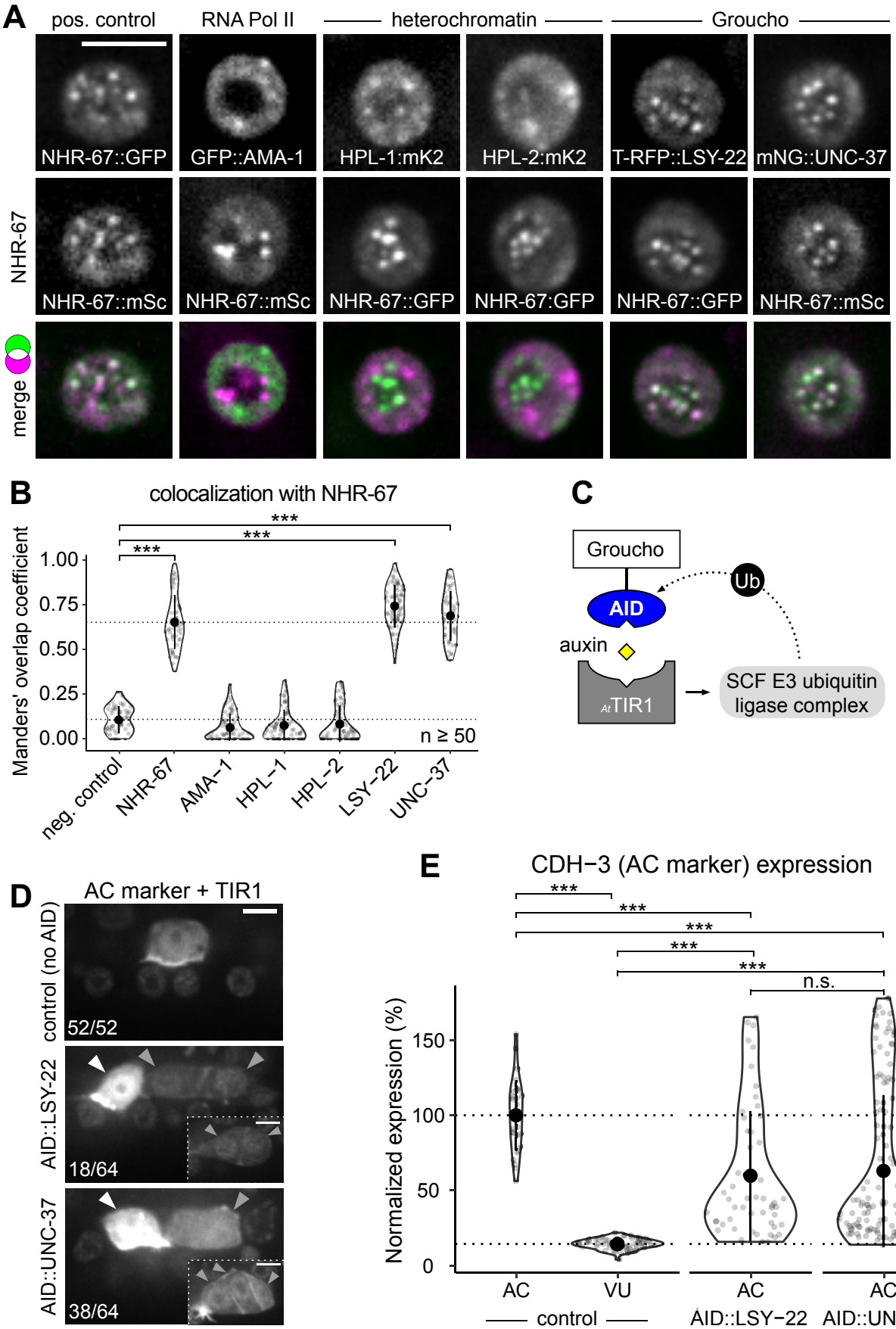

Figure 4–figure supplement 1

Medwig-Kinney et al. (2023)

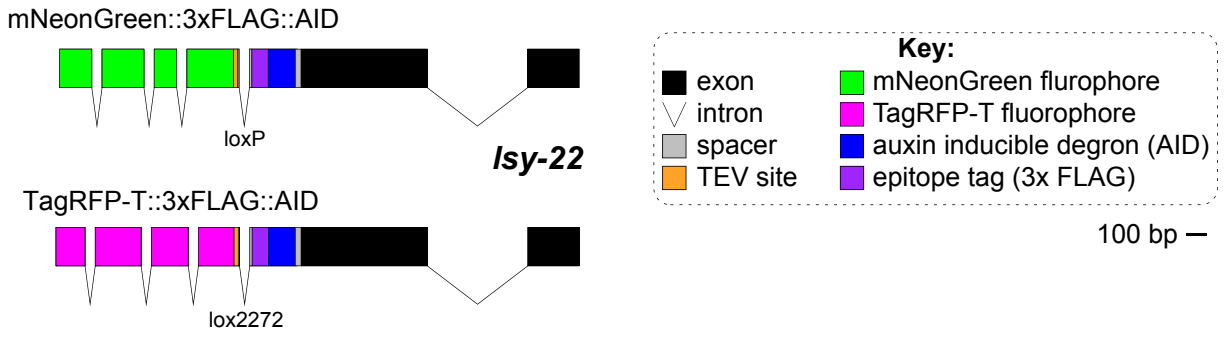

Figure 4–figure supplement 2 Medwig-Kinney et al. (2023)

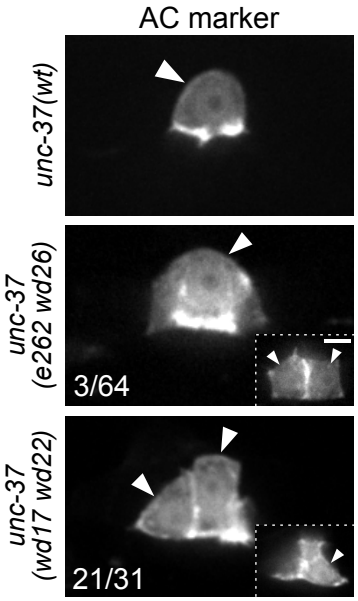

Figure 5 Medwig-Kinney et al. (2023)

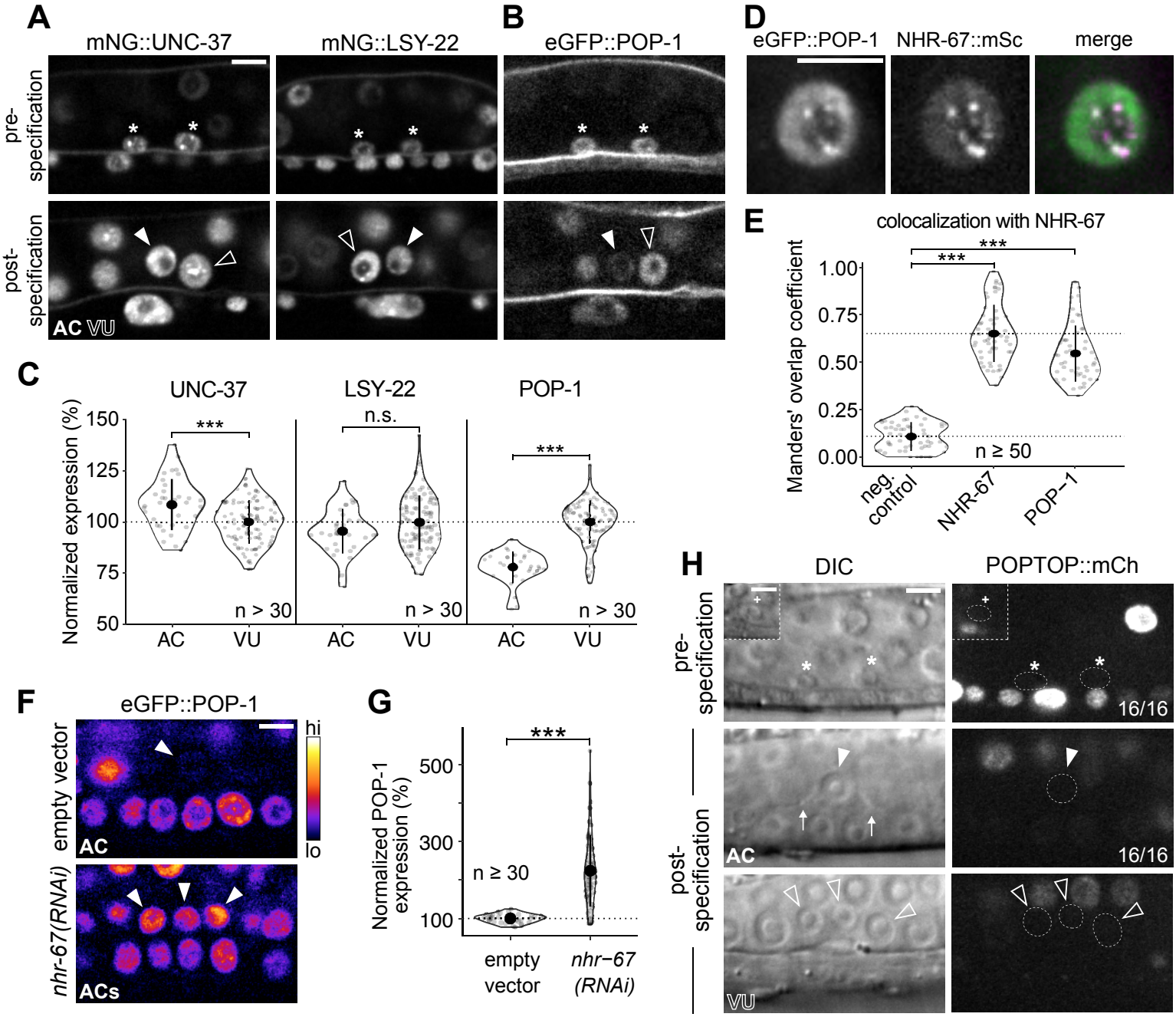

Figure 5–figure supplement 1 Medwig-Kinney et al. (2023)

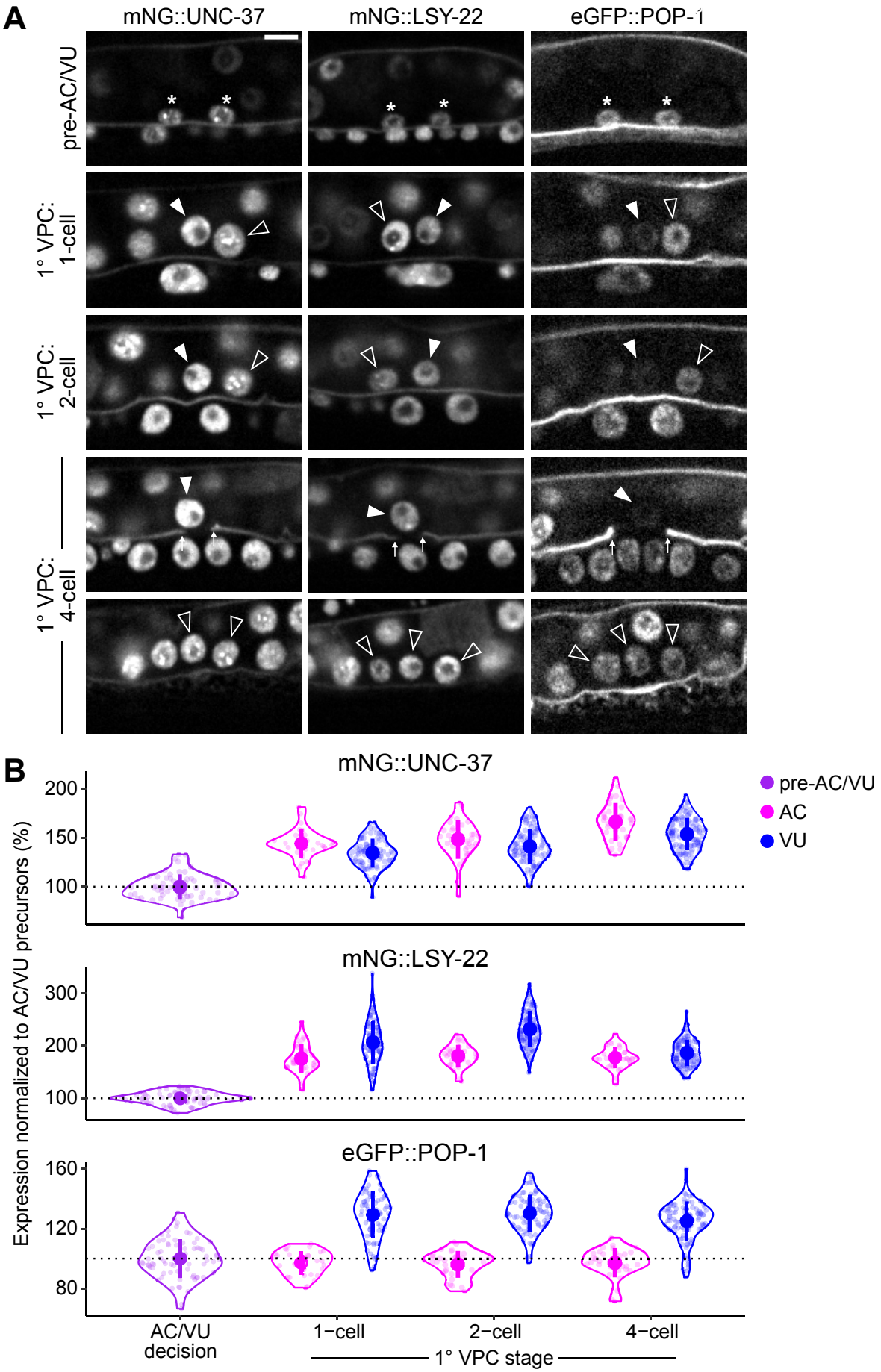

Figure 5–figure supplement 2

Medwig-Kinney et al. (2023)

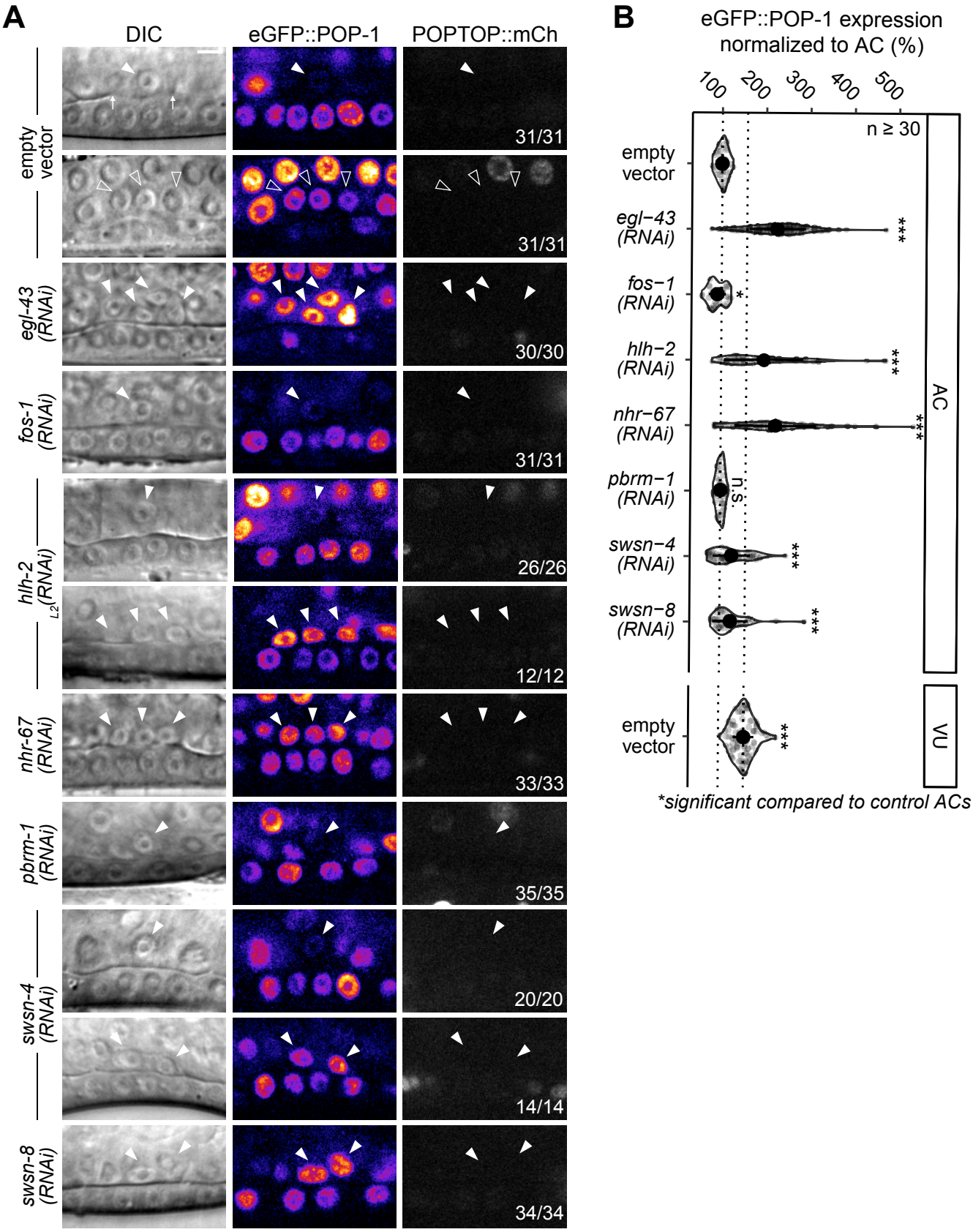

Figure 5–figure supplement 3 Medwig-Kinney et al. (2023)

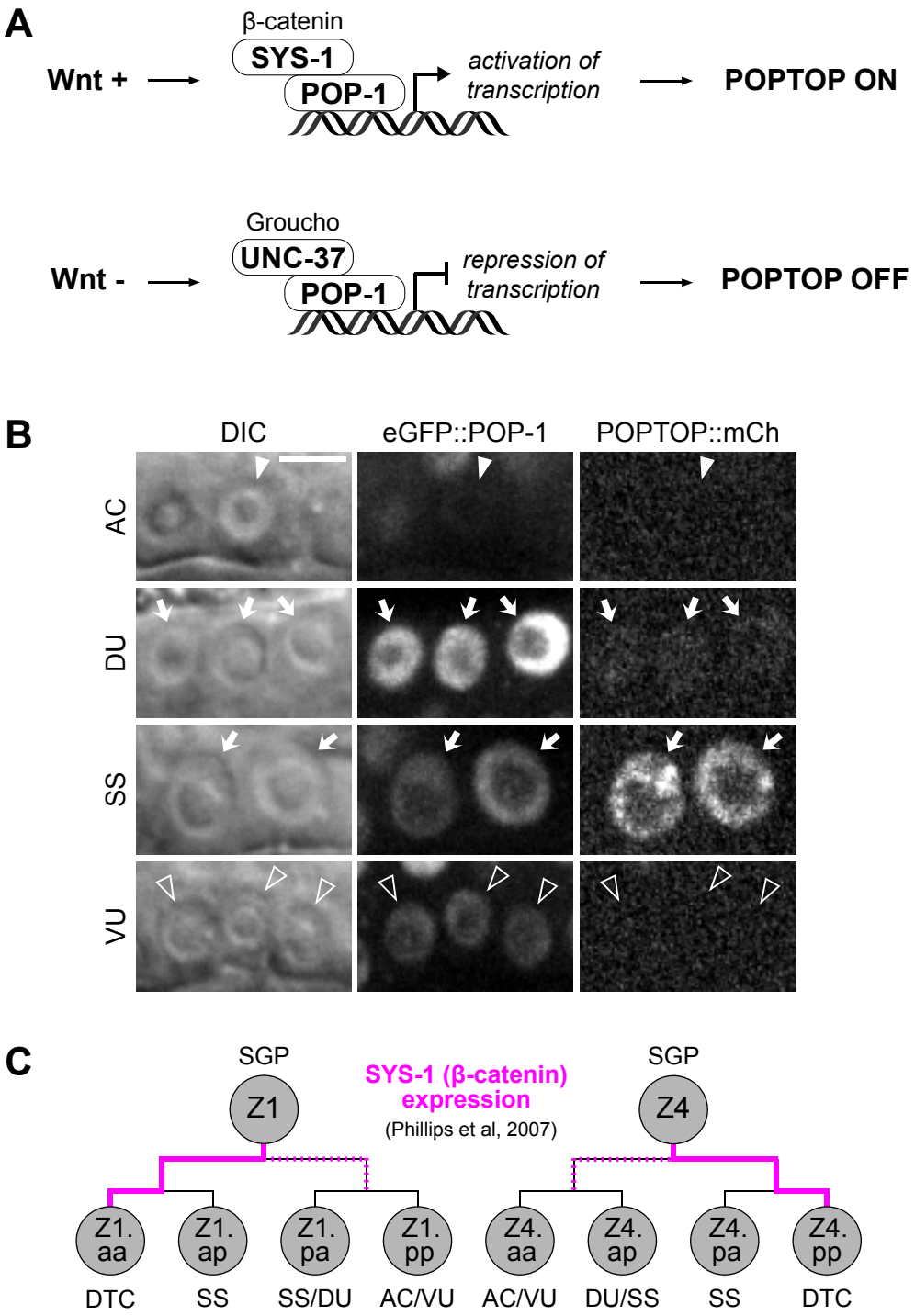

Figure 6 Medwig-Kinney et al. (2023)

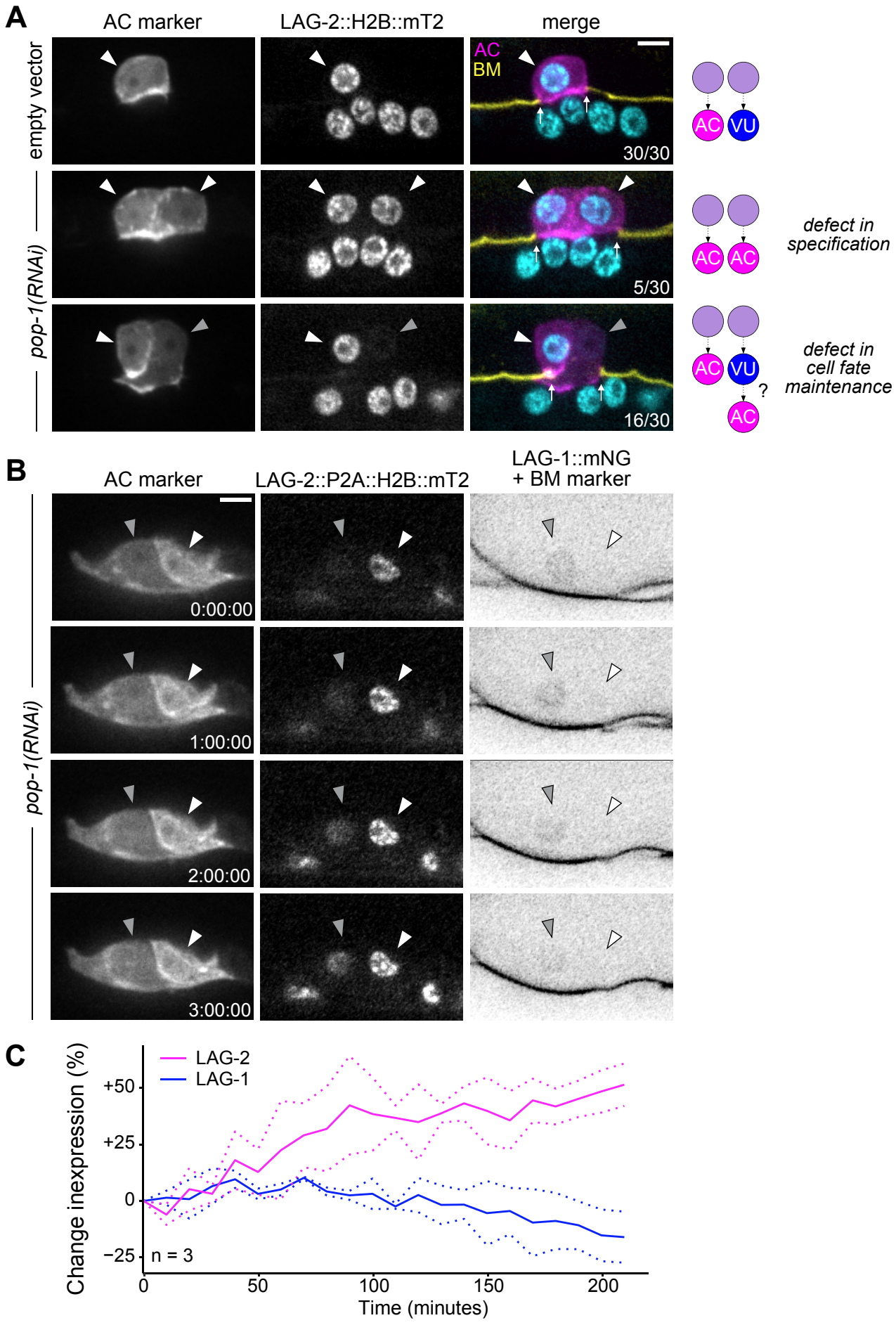

Figure 6–figure supplement 1

Medwig-Kinney et al. (2023)

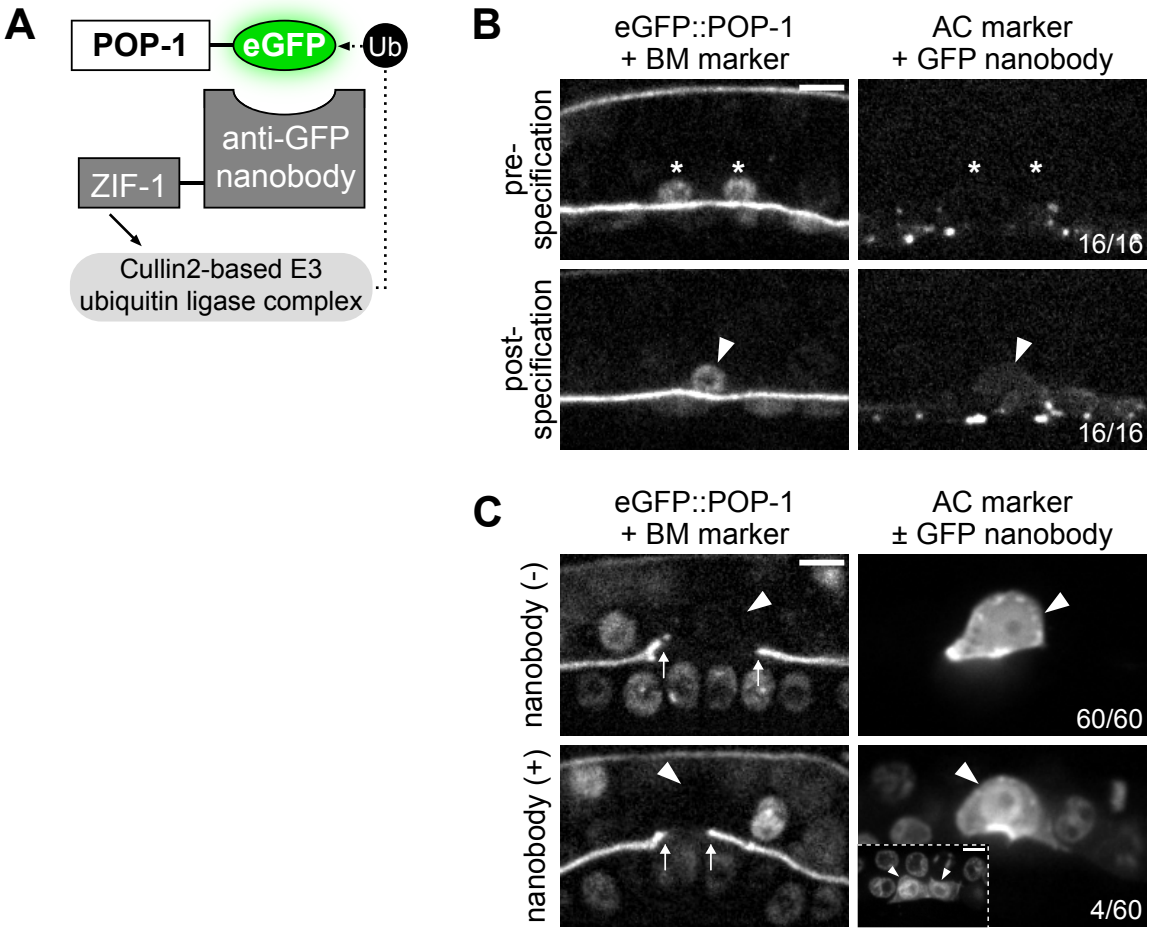

Figure 6–figure supplement 2 Medwig-Kinney et al. (2023)

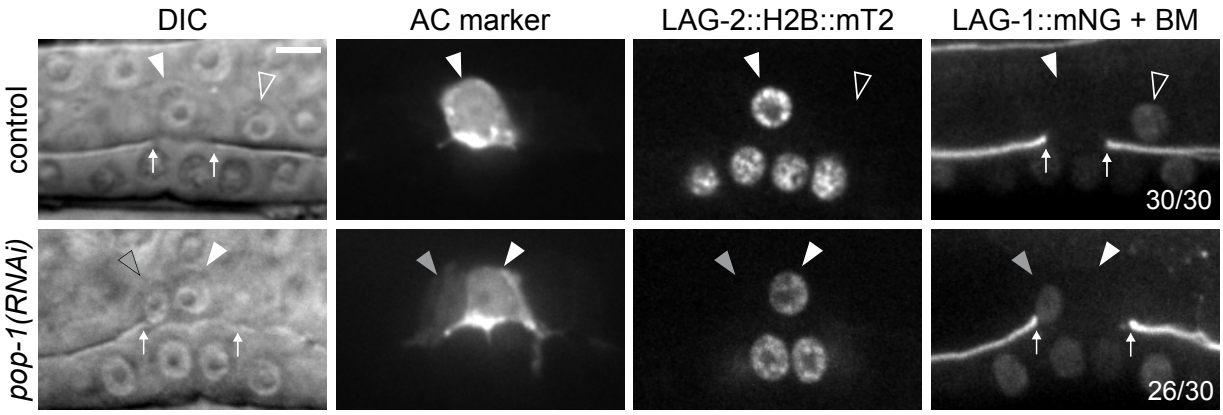

Figure 7 Medwig-Kinney et al. (2023)

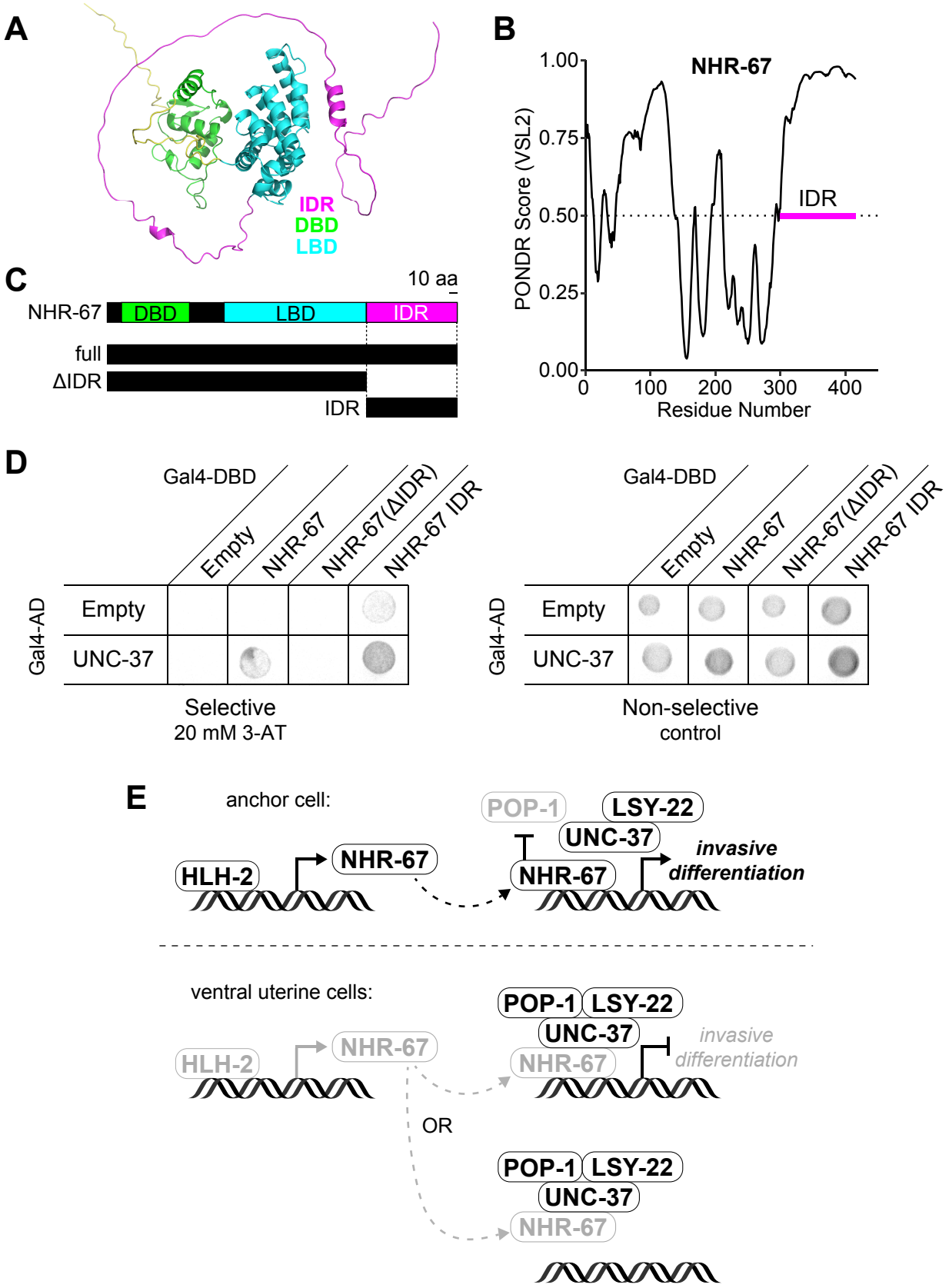
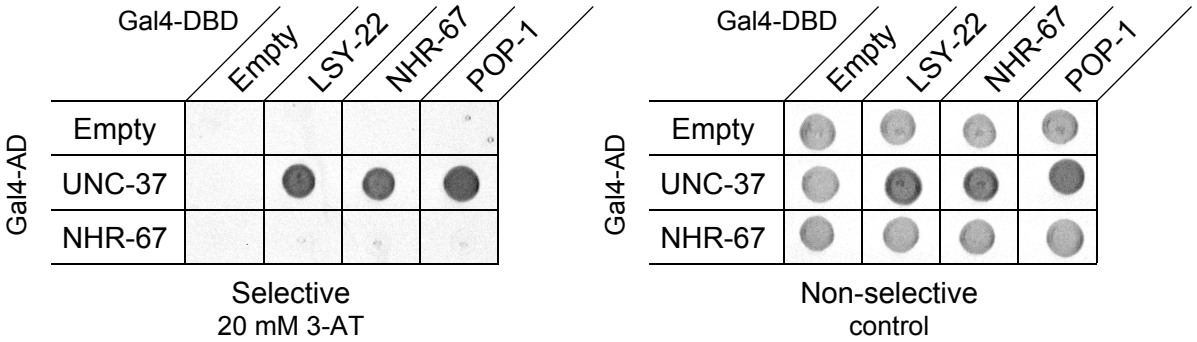
Figure 7–figure supplement 1 Medwig-Kinney et al. (2023)